

Galaxy And Mass Assembly (GAMA): a deeper view of the mass, metallicity and SFR relationships

M. A. Lara-López,¹★† A. M. Hopkins,¹ A. R. López-Sánchez,^{1,2} S. Brough,¹
M. L. P. Gunawardhana,^{1,3} M. Colless,¹ A. S. G. Robotham,^{4,5} A. E. Bauer,¹
J. Bland-Hawthorn,³ M. Cluver,¹ S. Driver,^{4,5} C. Foster,⁶ L. S. Kelvin,^{4,5,7}
J. Liske,⁸ J. Loveday,⁹ M. S. Owers,¹ T. J. Ponman,¹⁰ R. G. Sharp,¹¹ O. Steele,¹²
E. N. Taylor^{3,13} and D. Thomas¹²

¹Australian Astronomical Observatory, PO Box 915, North Ryde, NSW 1670, Australia

²Department of Physics and Astronomy, Macquarie University, NSW 2109, Australia

³Sydney Institute for Astronomy (SIfA), School of Physics, University of Sydney, NSW 2006, Australia

⁴School of Physics & Astronomy, University of St Andrews, North Haugh, St Andrews KY16 9SS, UK

⁵International Centre for Radio Astronomy Research, The University of Western Australia, 35 Stirling Highway, Crawley, WA 6009, Australia

⁶European Southern Observatory, Alonso de Cordova 3107, Vitacura, Santiago de Chile, Chile

⁷Institut für Astro- und Teilchenphysik, Universität Innsbruck, Technikerstraße 25, A-6020 Innsbruck, Austria

⁸European Southern Observatory, Karls-Schwarzschild-Str. 2, D-85748 Garching, Germany

⁹Astronomy Centre, University of Sussex, Falmer, Brighton BN1 9QH, UK

¹⁰School of Physics and Astronomy, University of Birmingham, Edgbaston, Birmingham B15 2TT, UK

¹¹Research School of Astronomy & Astrophysics, Australian National University, Cotter Road, Weston Creek, ACT 2611, Australia

¹²Institute of Cosmology and Gravitation, University of Portsmouth, Dennis Sciama Building, Burnaby Road, Portsmouth PO1 3FX, UK

¹³School of Physics, The University of Melbourne, Parkville, VIC 3010, Australia

Accepted 2013 June 7. Received 2013 June 5; in original form 2012 November 4

ABSTRACT

A full appreciation of the role played by gas metallicity (Z), star formation rate (SFR) and stellar mass (M_*) is fundamental to understanding how galaxies form and evolve. The connections between these three parameters at different redshifts significantly affect galaxy evolution, and thus provide important constraints for galaxy evolution models. Using data from the Sloan Digital Sky Survey–Data Release 7 (SDSS–DR7) and the Galaxy and Mass Assembly (GAMA) surveys, we study the relationships and dependences between SFR, Z and M_* , as well as the Fundamental Plane for star-forming galaxies. We combine both surveys using volume-limited samples up to a redshift of $z \approx 0.36$. The GAMA and SDSS surveys complement each other when analysing the relationships between SFR, M_* and Z . We present evidence for SFR and metallicity evolution to $z \sim 0.2$. We study the dependences between SFR, M_* , Z and specific SFR (SSFR) on the M_* – Z , M_* –SFR, M_* –SSFR, Z –SFR and Z –SSFR relations, finding strong correlations between all. Based on those dependences, we propose a simple model that allows us to explain the different behaviour observed between low- and high-mass galaxies. Finally, our analysis allows us to confirm the existence of a Fundamental Plane, for which $M_* = f(Z, \text{SFR})$ in star-forming galaxies.

Key words: galaxies: abundances – galaxies: evolution – galaxies: fundamental parameters – galaxies: star formation – galaxies: statistics.

1 INTRODUCTION

The star formation history and chemical enrichment are two of the main parameters that drive the evolution of galaxies. A detailed

appreciation of those properties spanning several cosmological epochs will provide stringent constraints on how galaxies form and evolve.

The stellar mass (M_*), star formation rate (SFR) and gas metallicity (Z) have been related in the past through the well-known mass–metallicity (M_* – Z) (e.g. Lequeux et al. 1979; Tremonti et al. 2004) and mass–SFR (M_* –SFR) relationships (e.g. Noeske et al. 2007; Brinchmann, Pettini & Charlot 2008). Also, it has been shown that

★ E-mail: mlopez@ao.gov.au

† ARC Super Science Fellow.

there is no strong correlation directly between the metallicity and SFR in galaxies (e.g. Lara-López et al. 2010a; López-Sánchez 2010; Yates, Kauffmann & Guo 2012).

The M_* – Z relation quantifies how the mass and metallicity of galaxies are related, with massive galaxies showing higher metallicities than less massive galaxies. Since metallicity is a tracer of the fraction of baryonic mass that has been converted into stars and is sensitive to the metal losses due to stellar winds, supernovae and active galactic nucleus (AGN) feedback, the M_* – Z relation provides essential insight into galaxy formation and evolution. The M_* – Z relation has been extensively studied in the local universe (e.g. Lequeux et al. 1979; Tremonti et al. 2004; Kewley & Ellison 2008, among others). With the advent of integral field spectroscopy (IFS) surveys, new results on the origin of the M_* – Z relation have been explored. Recently, Rosales-Ortega et al. (2012) demonstrate the existence of a local M_* – Z relation using 2572 spatially resolved H II regions in 38 galaxies. Furthermore, Sanchez et al. (2013) obtain the same local M_* – Z relation using the Calar Alto Legacy Integral Field Area Survey IFS data.

Metallicity has been shown to evolve to lower values even out to relatively low redshifts of $z \approx 0.4$ (e.g. Lara-López et al. 2009a, 2009b; Pilyugin & Thuan 2011). As redshift increases, the metallicity evolution is stronger. All studies of the M_* – Z relation in high-redshift ($z \sim 0.7$) galaxies have shown an evolution in metallicity with respect to local galaxies (Hammer et al. 2005; Maier et al. 2005; Savaglio et al. 2005; Liang et al. 2006; Rodrigues et al. 2008). At redshift $z \sim 2.2$, Erb et al. (2006) found that galaxies have a lower metallicity by ~ 0.3 dex, while at redshift $z \sim 3.5$, Maiolino et al. (2008) reported a strong metallicity evolution, suggesting that this redshift corresponds to an epoch of major star formation activity. The M_* – Z relation has also been studied for different morphological galaxy types. In particular, Calura et al. (2009) found that, at any redshift, elliptical galaxies have the highest stellar masses and the highest stellar metallicities, whereas the least massive and chemically unevolved objects are the irregular galaxies, see also Pilyugin et al. (2013) for an observational result.

There are two main ways to explain the origin of the M_* – Z relation. The first is attributed to metal and baryon loss due to gas outflow, where low-mass galaxies eject large amounts of metal-enriched gas by supernovae winds before high metallicities are reached, while massive galaxies have deeper gravitational potentials that retain their gas, thus reaching higher metallicities (Larson 1974; Dekel & Silk 1986; Mac Low & Ferrara 1999; De Lucia, Kauffmann & White 2000; Maier, Meisenheimer & Hippelein 2004; Tremonti et al. 2004; Kobayashi, Springel & White 2007; Finlator & Davé 2008). As pointed out in the high-resolution simulations of Brooks et al. (2007), supernovae feedback plays a crucial role in lowering the star formation efficiency in low-mass galaxies. Without energy injection from supernovae to regulate the star formation, gas that remains in galaxies rapidly cools, forms stars and increases the metallicity too early, producing an M_* – Z relation too flat compared to observations.

A second scenario to explain the M_* – Z relation is related to the well-known effect of downsizing (e.g. Cowie et al. 1996; Gavazzi & Scodreggio 1996), in which lower mass galaxies form their stars later and on longer time-scales than more massive systems, implying low star formation efficiencies in low-mass galaxies (e.g. Efstathiou 2000; Brooks et al. 2007; Ellison et al. 2008; Mouhcine et al. 2008; Tassis, Kravtsov & Gnedin 2008; Scannapieco et al. 2008). Therefore, low-mass galaxies are expected to show lower metallicities. Supporting this scenario, Calura et al. (2009) reproduced the M_* – Z relation with chemical evolution models for ellipticals, spirals and

irregular galaxies, by means of an increasing efficiency of star formation with mass in galaxies of all morphological types, without the need for outflows favouring the loss of metals in the less massive galaxies. Also, Vale Asari et al. (2009) modelled the time evolution of stellar metallicity using a closed-box chemical evolution picture, suggesting that the M_* – Z relation for galaxies in the mass range from $10^{9.8}$ to $10^{11.65} M_\odot$ is mainly driven by the star formation history and not by inflows or outflows.

The SFR is a key parameter to understand the stellar evolution. The hydrogen Balmer lines (mainly, the H α line) are one of the most reliable tracers of star formation (e.g. Moustakas, Kennicutt & Tremonti 2006), since the Balmer emission-line luminosity scales directly with the total ionizing flux of the embedded stars in H II regions and star-forming (SF) galaxies. It is important, however, to take into account corrections for stellar absorption and obscuration to obtain SFRs in agreement with those derived using other wavelengths (e.g. Charlot et al. 2002; Dopita et al. 2002; Rosa-González, Terlevich & Terlevich 2002; Hopkins et al. 2003).

A strong dependence of the SFR with the stellar mass, as well as its evolution with redshift has been found, with the bulk of star formation occurring first in massive galaxies, and later in less massive systems (Guzmán et al. 1997; Brinchmann & Ellis 2000; Bauer et al. 2005; Bell et al. 2005; Feulner et al. 2005; Juneau et al. 2005; Pérez-González et al. 2005; Caputi et al. 2006; Erb et al. 2006; Papovich et al. 2006; Reddy et al. 2006; Noeske et al. 2007; Buat et al. 2008). In the local universe, several studies have illustrated a relationship between the SFR and stellar mass, identifying two populations: galaxies on a SF sequence, and ‘quenched’ galaxies, with little or no detectable star formation (Brinchmann et al. 2004; Salim et al. 2005). At higher redshift, Noeske et al. (2007) showed the existence of a ‘main sequence’ (MS) for SF galaxies in the M_* –SFR relation over the redshift range $0.2 < z < 1.1$. Noeske et al. (2007) show that the slope of the MS remains constant to $z > 1$, while the MS as a whole moves to higher SFR as z increases.

The existence of Fundamental Planes (FP) is a natural result of scaling relationships between important astrophysical properties. The first study proposing a relationship between these three fundamental quantities was by Ellison et al. (2008) who found an SFR dependence on the M_* – Z relation for SF galaxies using data from the SDSS. An FP was found by Lara-López et al. (2010b) in a three-dimensional study of the M_* gas metallicity, and SFR of SF galaxies using data from the SDSS–DR7. Lara-López et al. (2010b) showed that the M_* – Z and M_* –SFR relationships are particular cases of a more general relationship, an FP. This combination reduces the scatter significantly compared to any other pair of correlations. In a parallel study, Mannucci et al. (2010) found similar fundamental 3D relationships, fitting a surface to the stellar mass, SFR and gas metallicity. Mannucci et al. (2010) provided an expression, referred to as the Fundamental Metallicity Relation, in which Z is expressed as a combination of M_* and SFR. In this regard, Yates et al. (2012) used SF galaxies from the SDSS–DR7 to study the dependences of the different combinations of SFR, metallicity and stellar mass. These authors found that, although having high dispersion, there is a dependence of M_* on the Z –SFR relation, and they obtained similar dependences using models. Yates et al. (2012) also found that the fit given by Mannucci et al. (2010) does not significantly reduce the dispersion of the metallicity compared to the M_* – Z relation.

Just in the past few years, many studies have attempted to quantify the distribution of galaxies in this three-dimensional space (Magrini et al. 2012; Peebles & Somerville 2013). Through testing a variety of different methodologies, Lara-López, López-Sánchez & Hopkins

(2013b) conclude that a planar distribution is sufficient to account for 98 per cent of the variance in the $M_* - ZSFR$ space.

This paper is structured as follows. In Section 2, we detail the data used for this study. In Section 3, we analyse the evolution of the SFR, specific SFR (SSFR) and metallicity for our sample of galaxies. In Section 4, we investigate the FP for GAMA and SDSS galaxies. In Section 5, we present the different dependences of SFR, metallicity and M_* . Finally, in Section 6, we give a summary and conclusions. Throughout we assume $H_0 = 70 \text{ km s}^{-1} \text{ Mpc}^{-1}$, $\Omega_M = 0.3$, $\Omega_\Lambda = 0.7$.

2 SAMPLE SELECTION

We consider emission-line galaxies from two large surveys, the ‘Galaxy and Mass Assembly’ (GAMA) survey (Driver et al. 2011), and the ‘Sloan Digital Sky Survey–Data Release 7’ (SDSS–DR7) (Adelman-McCarthy et al. 2007; Abazajian et al. 2009).

GAMA is a spectroscopic survey based on data taken with the 3.9 m Anglo-Australian Telescope using the 2dF fibre feed and AAOmega multi-object spectrograph (Sharp et al. 2006). The spectra were taken with 2 arcsec diameter fibre, a spectral coverage from 3700 to 8900 Å, and spectral resolution of 3.2 Å. In this study, we use the GAMA phase-I survey, which covers three fields of 48 deg², with Petrosian magnitude limits of $m_r < 19.8$ mag in one field and $m_r < 19.4$ mag in the other two. The GAMA data used in this paper include spectra of $\sim 140\,000$ galaxies. Our main galaxy sample for GAMA is composed of galaxies in the range $17.77 < m_r < 19.8$ and redshifts up to $z \approx 0.36$.

Emission lines for the GAMA survey are measured in two ways. As a first approach, we fit Gaussians to a selection of common emission lines at appropriate observed wavelengths, given the measured redshift of each object. The local continuum spanning each fitted region is approximated with a linear fit. A second approach uses the Gas AND Absorption Line Fitting algorithm (GANDALF; Sarzi et al. 2006) to measure emission lines for the GAMA galaxies. GANDALF is a simultaneous emission and absorption line fitting algorithm designed to separate the relative contribution of the stellar continuum and of nebular emission in the spectra of galaxies, while measuring the gas emission and kinematics. GANDALF measures and corrects for dust attenuation and stellar absorption in the emission lines. The final set of measurements for both methods includes the flux, equivalent width (EW) and signal-to-noise ratio (SNR) for each emission line, among other results. Both measurements show good agreement between the independent approaches (Hopkins et al. 2013).

For SFR estimations the first approach is used. The H α line is measured directly from the flux-calibrated spectra, corrected for dust using the Balmer decrements and for stellar absorption as detailed by Brough et al. (2011) and Gunawardhana et al. (2011). For metallicity measurements, we use the GANDALF catalogue. The GANDALF measurements account for the stellar absorption in the Balmer lines through the SED fitting. This does not improve the SFR estimates, due to the approach taken in making obscuration corrections within GANDALF, but it does provide the most robust estimate of the adjacent line ratios used in the metallicity estimates.

Data from the SDSS were taken with a 2.5 m telescope located at Apache Point Observatory (Gunn et al. 2006). The SDSS spectra were obtained using 3 arcsec diameter fibres, covering a wavelength range of 3800–9200 Å, a spectral resolution $\lambda/\Delta\lambda \sim 1800$ –2200 and a wavelength coverage from 3800 to 9200 Å. The SDSS–DR7 spectroscopy data base contains spectra for $\sim 1.6 \times 10^6$ objects,

including 929 555 galaxies over $\sim 9380 \text{ deg}^2$. Further technical details can be found in Stoughton et al. (2002).

We used the emission-line analysis of SDSS–DR7 galaxy spectra from the Max-Planck-Institute for Astrophysics–John Hopkins University (MPA–JHU) data base.¹ Apparent and absolute Petrosian magnitudes were taken from the STARLIGHT data base² (Cid Fernandes et al. 2005, 2007; Mateus et al. 2006; Asari et al. 2007). From the full data set, we only consider objects classified as galaxies in the ‘main galaxy sample’ (Strauss et al. 2002) with apparent Petrosian r magnitude in the range $14.5 < m_r < 17.77$.

According to Kewley, Jansen & Geller (2005), a minimum of 20 per cent of the galaxy light inside the optical fibre is needed to avoid any possible bias due to the fibre diameter. Hence, we imposed a lower redshift limit of $z = 0.04$ and $z = 0.07$ for data from the SDSS and GAMA samples, respectively. The redshift difference is due to the different fibre diameters used in each survey. With these redshift limits any metallicity biases due to the fibre aperture sampling only the central regions of a galaxy should be minimized.

From the GAMA and SDSS samples described above, we construct volume-limited samples by selecting narrow redshift bins of equal absolute Petrosian r -band magnitudes, as shown in Figs 1(a) and (b), and Table 1. To construct the volume-limited samples, we used the full data samples of both surveys. The red line in both panels of Fig. 1 shows the apparent Petrosian r -band bright/faint limit for GAMA/SDSS, respectively, corresponding to $m_r = 17.77$. The blue line for the GAMA sample, Fig. 1(b), corresponds to the limit in apparent Petrosian magnitude $m_r = 19.8$, while for the SDSS sample, Fig. 1(a), the blue line corresponds to the limit of $m_r = 14.5$. The limits on the stellar mass of the volume-limited samples were determined as shown by the horizontal blue lines in Fig. 2.

For both galaxy surveys, we select all galaxies for which data in each of the H α , H β , [N II] $\lambda 6584$ and [O III] $\lambda 5007$ emission lines are available. We obtain a total of 85 378 and 632 652 for the GAMA and SDSS surveys, respectively. Our next step is to select only SF galaxies and not objects with some kind of nuclear activity (e.g. composite and AGN galaxies). To this end, we use the BPT diagram (Baldwin, Phillips & Terlevich 1981) that compares the [O III] $\lambda 5007/\text{H}\beta$ and [N II] $\lambda 6584/\text{H}\alpha$ ratios (Fig. 3). We also impose an SNR higher than 3σ for H α , H β and [N II]. This last criterion results in 455 872 objects for SDSS and 28 238 galaxies for GAMA.

From this sample, we classify the objects into SF, composites and AGN galaxies following the criteria of Kauffmann et al. (2003a) and Kewley et al. (2001). The corresponding percentage of SF, composite and AGN galaxies for GAMA is 79.3, 9.3 and 11.4 per cent, respectively, while for SDSS it is 66.5, 21.9 and 11.5 per cent, respectively. Fig. 3 shows the BPT diagram for both samples. This figure also includes a histogram showing the percentage of SF, composites and AGN galaxies for both surveys. The GAMA survey has more SF galaxies than SDSS because GAMA is deeper than the SDSS and more sensitive to low-mass systems at low redshift, which are more dominated by star formation than AGN activity.

Kelvin et al. (2012) estimate the Sérsic indexes (n) for galaxies in the GAMA survey via a detailed and independent modelling in the $ugriz$, Y , J , H & K bands. Kelvin et al. (2012) report a bimodality, with two Gaussian-like distributions in most of the bands. For the r band there is a rough separation at $n \approx 1.9$ [$\log(n) \approx 0.278$] between early- and late-type galaxies. Based on the Sérsic index, 86 per cent

¹ <http://www.mpa-garching.mpg.de/SDSS/>

² <http://www.starlight.ufsc.br>

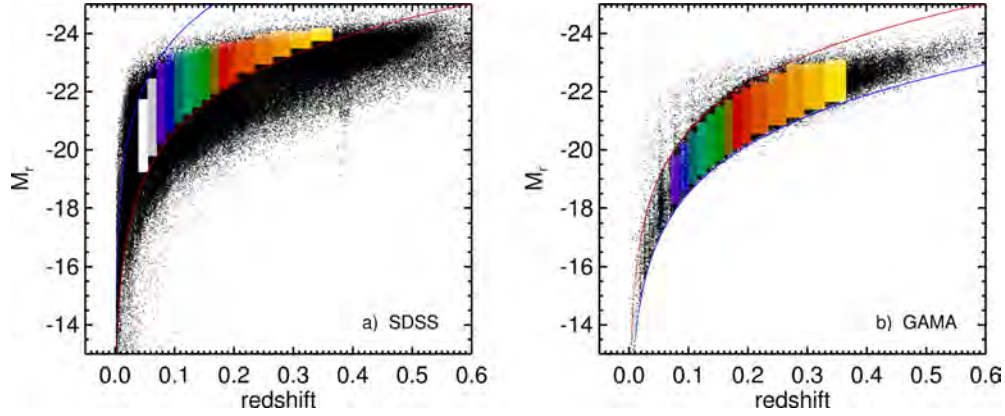


Figure 1. Redshift versus Petrosian r -band absolute magnitude (M_r) for the (a) SDSS and (b) GAMA surveys. The red line is the same in both plots, and corresponds to the bright/faint apparent r -magnitude (m_r) limit of 17.77 for GAMA/SDSS. The blue lines correspond, respectively, to the SDSS m_r limit of 14.5, and to the GAMA m_r limit of 19.8. The colour boxes correspond to each of the volume-limited samples, where the same colours represent the same redshift bins, but different magnitudes for each survey. Note that the white and grey boxes in the SDSS sample correspond to redshifts $0.04 < z < 0.07$ that do not appear in the GAMA sample.

Table 1. Redshifts and r -band absolute Petrosian magnitude limits for the volume limited samples of the SDSS and GAMA surveys shown in Fig. 1.

| Sample | z_{\min} | z_{\max} | SDSS | | GAMA | |
|--------|------------|------------|---------------|---------------|---------------|---------------|
| | | | M_r (upper) | M_r (lower) | M_r (upper) | M_r (lower) |
| 1 | 0.04 | 0.055 | -19.248 | -21.734 | – | – |
| 2 | 0.055 | 0.07 | -19.795 | -22.448 | – | – |
| 3 | 0.070 | 0.085 | -20.239 | -22.995 | -18.139 | -19.795 |
| 4 | 0.085 | 0.1 | -20.615 | -23.439 | -18.515 | -20.239 |
| 5 | 0.1 | 0.115 | -20.950 | -23.439 | -18.850 | -20.615 |
| 6 | 0.115 | 0.130 | -21.227 | -23.5 | -19.127 | -20.950 |
| 7 | 0.130 | 0.145 | -21.485 | -23.6 | -19.385 | -21.227 |
| 8 | 0.145 | 0.160 | -21.719 | -23.6 | -19.619 | -21.485 |
| 9 | 0.160 | 0.175 | -21.933 | -23.7 | -19.833 | -21.719 |
| 10 | 0.175 | 0.190 | -22.131 | -23.7 | -20.031 | -21.933 |
| 11 | 0.190 | 0.205 | -22.316 | -23.7 | -20.216 | -22.131 |
| 12 | 0.205 | 0.235 | -22.649 | -23.8 | -20.549 | -22.316 |
| 13 | 0.235 | 0.265 | -22.946 | -24.0 | -20.846 | -22.649 |
| 14 | 0.265 | 0.295 | -23.213 | -24.1 | -21.113 | -22.946 |
| 15 | 0.295 | 0.330 | -23.494 | -24.1 | -21.394 | -23.0 |
| 16 | 0.330 | 0.365 | -23.750 | -24.2 | -21.650 | -23.1 |

of the GAMA-SF sample used in our study correspond to late-type galaxies (Fig. 4).

For the SDSS survey, global Sérsic indexes (n_g) were estimated by Simard et al. (2011) fitting simultaneous bulge+disc decompositions in g and r bands. These authors only provide a single Sérsic

index for both bands. A value of $n_g \sim 2$ [$\log(n) \approx 0.3$], gives a rough separation between the two distributions. According to this, 80 per cent of our SDSS-SF sample correspond to late-type galaxies (Fig. 4).

The distribution of the GAMA sample shows a similar Gaussian-bimodality between both populations of late- and early-type galaxies. However, since the SDSS is a survey of brighter galaxies, it shows a stronger early-type population of galaxies. There is a small systematic difference between the Sérsic indexes of both surveys due to the different estimation methods used. Nevertheless, both methods indicate that most of our SF sample correspond to late-type galaxies.

2.1 SFR, metallicity and stellar mass estimates

2.1.1 The SDSS sample

We use several methods to determine the gas-phase metallicities and SFRs for the SF galaxies of the SDSS survey. Metallicities were estimated using (i) the empirical calibration provided by Pettini & Pagel (2004) between the oxygen abundance and the O3N2 index (which is defined below); (ii) the calibration given by Kewley & Dopita (2002), with the update of Kewley & Ellison (2008), which is based on photoionization models and considers the $[\text{N II}]/[\text{O II}]$ ratio and (iii) the Tremonti et al. (2004) metallicities, which are also based on photoionization models and rely on Bayesian methods.

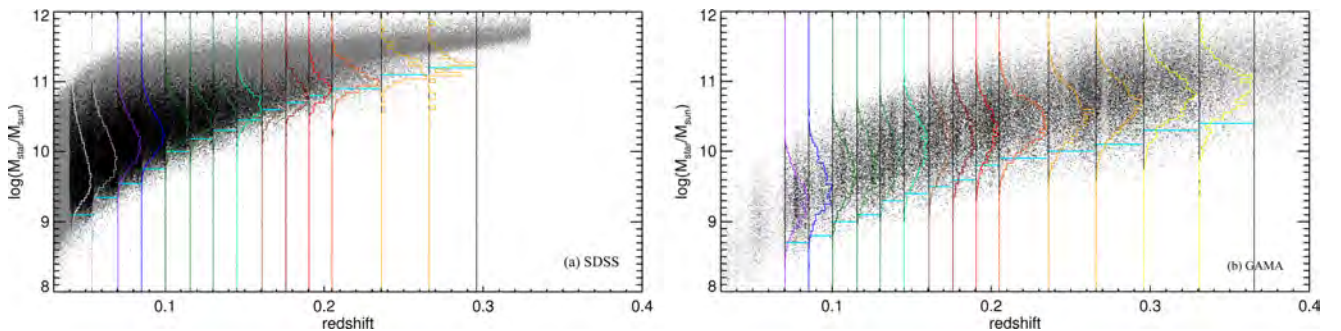


Figure 2. Redshift versus stellar mass for (a) SDSS and (b) GAMA. In both panels, grey dots show the full sample, while the black dots show only the volume-limited samples of Fig. 1. The vertical histograms in each plot correspond to galaxies in each volume-limited sample colour coded as in previous plot. Horizontal light blue lines correspond to the mass limit in each redshift bin.

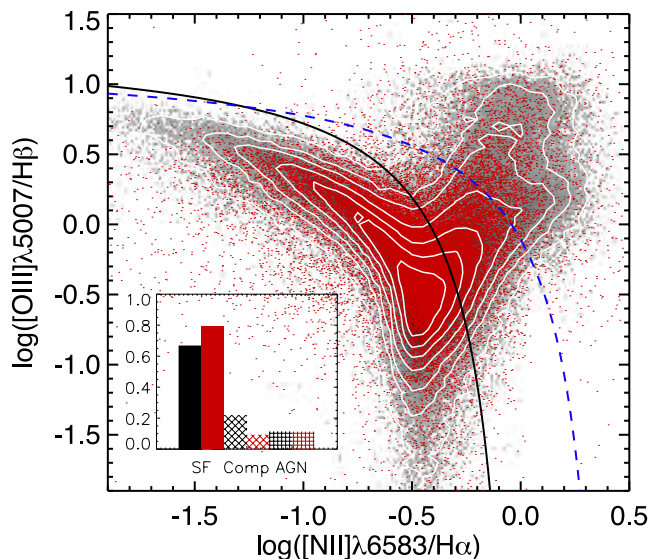


Figure 3. BPT (Baldwin et al. 1981) diagram for the SDSS and GAMA samples. The grey density plot and white contours correspond to the SDSS sample, while the red dots correspond to the GAMA sample. The solid line represents the empirical relation provided by Kauffmann et al. (2003a), and galaxies below this line correspond to SF galaxies. The dashed line corresponds to the Kewley et al. (2001) relation. Galaxies between the solid and dashed lines correspond to composite, while galaxies above the dashed line correspond to AGNs. The histogram shows the percentage of SF, composite and AGN galaxies for the SDSS (black) and the GAMA (red) samples.

We compare these three methods and find that the scatter in metallicity for the $M_* - Z$ relation is minimized when Tremonti et al. (2004) is used. Hereafter, we use those metallicities for the data from the SDSS sample. Tremonti et al. (2004) estimated metallicities statistically using Bayesian techniques based on simultaneous fits of the most prominent emission lines ($[\text{O II}]$, $\text{H}\beta$, $[\text{O III}]$, $\text{H}\alpha$, $[\text{N II}]$, $[\text{S II}]$), using a model designed for the interpretation of integrated galaxy spectra (Charlot & Longhetti 2001). Since the metallicities derived with this technique are discretely sampled, they exhibit small random offsets (for details see Tremonti et al. 2004).

We estimate SFRs using two different approaches. First, we use the method described by Hopkins et al. (2003), which uses the EW of the $\text{H}\alpha$ line. We correct the SFRs for stellar absorption, obscuration and aperture effects (see Section 2.1.2 for details). We also use Brinchmann et al. (2004), whose SFRs are based on Bayesian methods. A comparison between both SFRs shows a tight correlation (see Appendix A for details). While the SFRs derived using Hopkins et al. (2003) are robust, for the SDSS sample we choose to use the total SFRs of Brinchmann et al. (2004). As we show below, our results do not change significantly regardless of which SFR estimate we use. Brinchmann et al. (2004) estimated SFRs modelling the emission lines in the galaxies following the Charlot et al. (2002) prescription, achieving a robust dust correction. The metallicity dependence for the case B recombination in the $\text{H}\alpha/\text{H}\beta$ ratio is also taken into account.

Total stellar masses were estimated as in Kauffmann et al. (2003b), which relies on spectral indicators of the stellar age, and the fraction of stars formed in recent bursts. These authors used the z -band magnitude to characterize the galaxy luminosity and constrain the star formation history using both the 4000 Å break, $D_n(4000)$, and the stellar Balmer absorption, $\text{H}\delta_A$. The location of

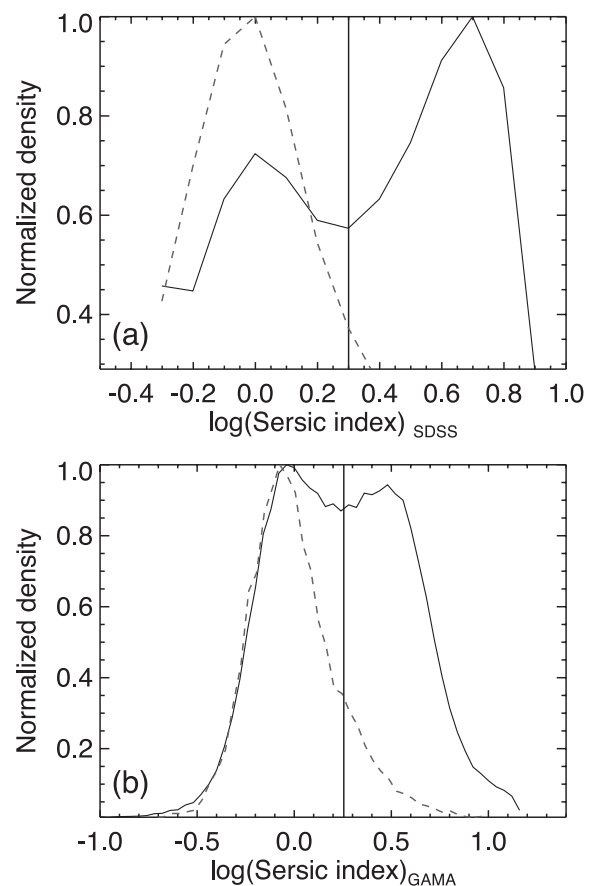


Figure 4. Normalized histograms of the Sérsic index for the whole galaxy sample of the (a) SDSS and (b) GAMA surveys. In both panels, the solid black line corresponds to the whole sample, while the dashed line corresponds to the SF sample. The vertical solid line indicates the limit between late- and early-type galaxies.

a galaxy in the $D_n(4000) - \text{H}\delta_A$ plane is insensitive to reddening and depends weakly on metallicity. A Kroupa (2001) stellar initial mass function (IMF) was assumed.

2.1.2 The GAMA sample

From the GAMA SF sample described in Section 2, we computed metallicities using the O3N2 parameter, which is defined as

$$\text{O3N2} \equiv \log \left(\frac{[\text{O III}] \lambda 5007 / \text{H}\beta}{[\text{N II}] \lambda 6583 / \text{H}\alpha} \right), \quad (1)$$

applying the calibration of Pettini & Pagel (2004):

$$[12 + \log(\text{O}/\text{H})]_{\text{PP04}} = 8.73 - 0.32 \times \text{O3N2}. \quad (2)$$

However, it is well known (e.g. López-Sánchez & Esteban 2010; Moustakas et al. 2010) that there is an offset of ~ 0.3 dex between the oxygen abundances derived using empirical calibrations such as this, which rely on direct estimations of the electron temperature of the ionized gas (Pettini & Pagel 2004) and those derived using photoionization models (Kewley & Dopita 2002) or Tremonti et al. (2004). This issue has been recently reviewed by López-Sánchez et al. (2012). Hence, to work in the same system as the MPA-JHU Bayesian estimates, we compute metallicities using equations (1) and (2) for the SDSS, and calibrate them to the Tremonti et al.

(2004) metallicities (T04), obtaining

$$[12 + \log(\text{O}/\text{H})]_{\text{T04}} = 0.1026 + 1.0211 \times [12 + \log(\text{O}/\text{H})]_{\text{PP04}}. \quad (3)$$

Following this equation, a galaxy with an oxygen abundance of $12 + \log(\text{O}/\text{H}) = 9.00$ derived following the Pettini & Pagel (2004) calibration would correspond to a metallicity of $12 + \log(\text{O}/\text{H}) = 9.29$ from the Tremonti et al. (2004) method. See Appendix A for details of this calibration, and Appendix B for a comparison between GAMA and SDSS metallicities. For an analysis of metallicity errors and signal-to-noise effects for the GAMA sample, see Foster et al. (2012).

SFRs were estimated using the prescription of Hopkins et al. (2003) which relies on the $\text{EW}_{\text{H}\alpha}$, and corrected for obscuration, stellar absorption and fibre aperture as follows:

$$\text{SFR}_{\text{Hopkins}} = \frac{L_{\text{H}\alpha}}{1.27 \times 10^{34}}, \quad (4)$$

where $L_{\text{H}\alpha}$ corrected by stellar absorption and dust obscuration is given by

$$L_{\text{H}\alpha} = (\text{EW}_{\text{H}\alpha} + \text{EW}_c) \times 10^{-0.4(M_r - 34.10)} \times \frac{3 \times 10^{18}}{[6564.61(1+z)]^2} \times \left(\frac{F(\text{H}\alpha)_{\text{obs}}/F(\text{H}\beta)_{\text{obs}}}{2.86} \right)^{2.36} \quad (5)$$

and $F(\text{H}\alpha)$ and $F(\text{H}\beta)$ are the observed emission line fluxes of $\text{H}\alpha$ and $\text{H}\beta$, respectively. EW_c corresponds to a fixed absorption stellar correction of 0.7 (Gunawardhana et al. 2011) and M_r is the absolute Petrosian magnitude (for a detailed discussion, see Hopkins et al. 2003).

To work in the same system as the MPA–JHU Bayesian estimates used for the SDSS data, we computed SFRs using equations (4) and (5) for the SDSS data, and calibrated them to the Brinchmann et al. (2004) SFRs system, obtaining

$$\log(\text{SFR})_{\text{B04}} = -0.0648 + 1.3759 \times \log(\text{SFR})_{\text{Hopkins}}. \quad (6)$$

See Appendix 1 for more details. It is important to note that the estimated SFRs have been rescaled to a Kroupa (2001) IMF.

Finally, stellar masses were measured by Taylor et al. (2011), who estimate the stellar mass-to-light ratio (M_*/L) from optical photometry using stellar population synthesis models. They demonstrate that the relation between $(g - i)$ and M_*/L offers a simple indicator of the stellar masses. The stellar masses assume a Chabrier (2003) IMF. It is worth noting that the Chabrier (2003) and Kroupa (2001) IMFs have very similar shapes, and that the conversion factor between them when estimating stellar masses is negligible (e.g. Haas 2010).

2.1.3 Dust extinction correction

The extinction correction for our sample was derived using the Cardelli, Clayton & Mathis (1989) extinction law, based on observed Balmer decrements assuming Case B recombination. The relation between the observed and corrected fluxes is given by $F(\lambda)_{\text{corr}} = F(\lambda)_{\text{obs}} 10^{0.4 * A_\lambda}$, where $F(\lambda)_{\text{corr}}$ and $F(\lambda)_{\text{obs}}$ correspond to the corrected and observed fluxes, respectively.

Since GAMA is a fainter survey in magnitude than the SDSS, we expect, on average, larger extinction corrections. This comes about for two reasons. First, GAMA is sensitive to fainter systems than SDSS at similar redshift and luminosity, which are fainter due to being more heavily obscured. Secondly, GAMA is sensitive to

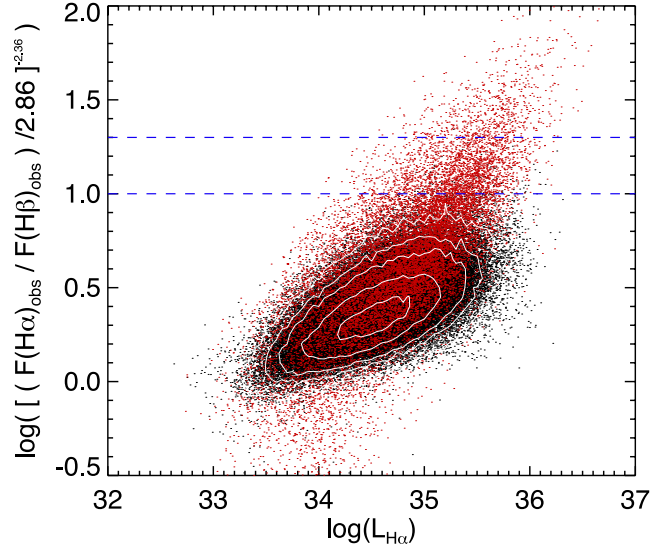


Figure 5. $\text{H}\alpha$ Luminosity versus reddening correction factor for SDSS (black) and GAMA (red) galaxies. Contours correspond to the SDSS sample. The blue dashed lines correspond to a reddening correction factor of 10 (Balmer decrement of 7.58) and 19.2 (Balmer decrement of 10).

high-SFR systems at higher redshift than SDSS, which have higher obscuration associated with their larger SFRs (e.g. Hopkins et al. 2003). As we are deriving metallicities through relatively close emission line ratios ($[\text{O III}]\lambda 5007/\text{H}\beta$ and $[\text{N II}]\lambda 6583/\text{H}\alpha$), the correction for extinction essentially cancels out. An overestimation of the extinction for the $\text{H}\alpha$ line, however, would result in an overestimation of the SFR, which may mislead our conclusions about the evolution of the SFR.

To avoid any spuriously high Balmer decrements introducing overestimated SFRs in our analysis, we imposed an upper limit of 10 to the obscuration correction, which results in a Balmer decrement of ~ 7.58 . We also compare our results taking an upper limit of ~ 19.2 to the obscuration correction, which corresponds to a Balmer decrement of 10. Those limits are shown in Fig. 5. The differences in SFR evolution are small, and will be studied in Section 3.

3 EVOLUTION OF THE SFR, SSFR, Z AND M_* RELATIONSHIPS FOR GAMA AND SDSS GALAXIES

In this section, we use a statistically robust sample combining both SDSS and GAMA galaxies in volume-limited samples up to $z \sim 0.36$ to explore possible evolution of the $M_* - Z$, $M_* - \text{SFR}$, $M_* - \text{SSFR}$ and $Z - \text{SFR}$ relationships. Figs 6–9 plot these relationships for the 16 volume-limited samples described in Section 2. In these figures, data from the SDSS are shown in black, while those from GAMA are shown in red. Both samples show good agreement in the internal consistency between the surveys, and in the overall trends. The large volume covered by the SDSS gives us a robust local fit for all our local relationships. For $z > 0.1$ the SDSS survey becomes more incomplete for lower mass galaxies; however, at this point, the GAMA sample fills in the lower mass populations. The evolution seen at high redshift is evident primarily in the GAMA survey.

For GAMA galaxies, samples 8 and 9 (marked with a star from Figs 6 to 9) will not be taken into account because they are strongly

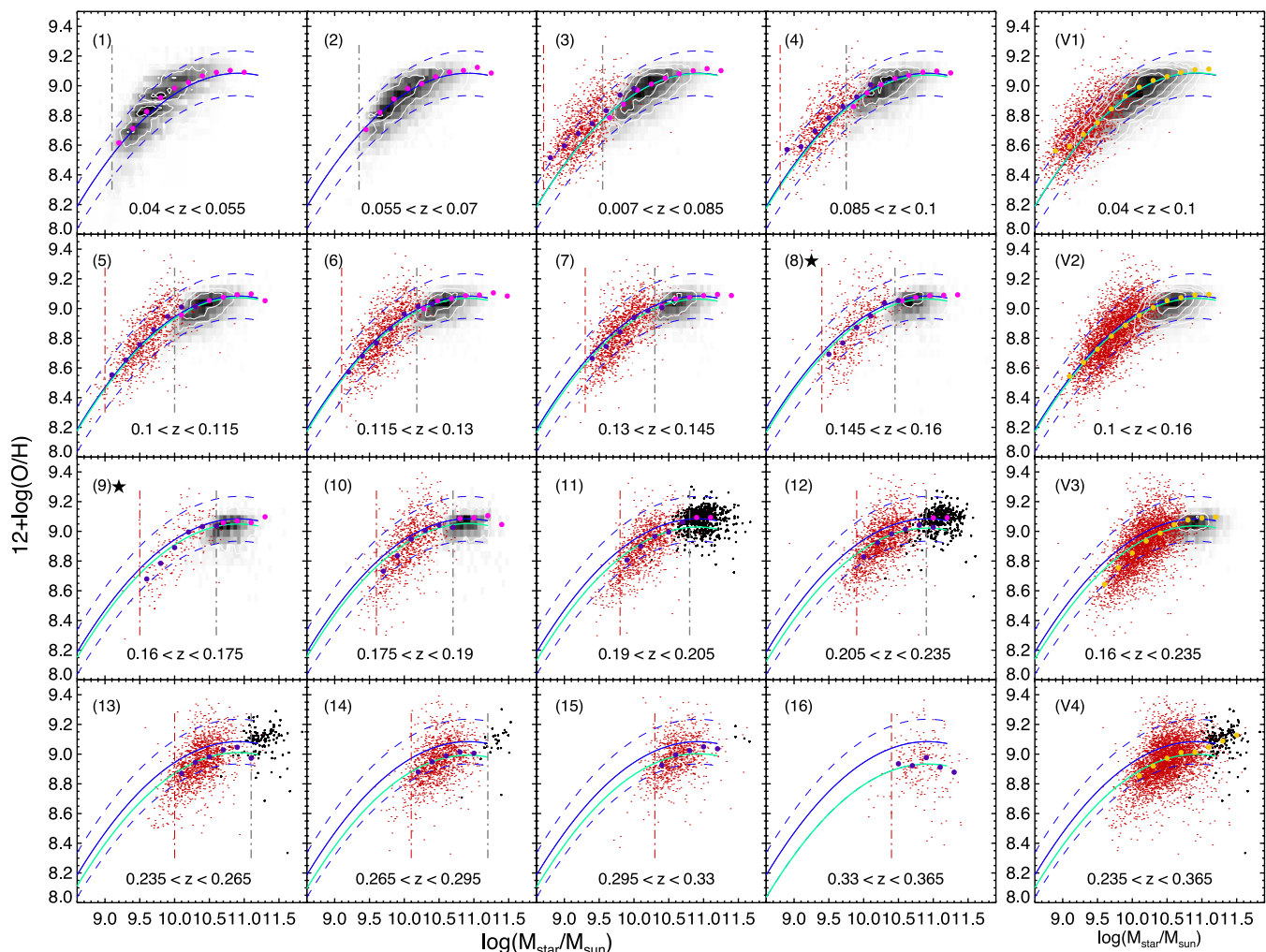


Figure 6. M_* – Z relation for our volume-limited galaxy samples using data from the GAMA (red dots) and SDSS (black dots) surveys. The redshift range used is shown at the bottom of each panel, and the number in the top-left corner of each panel identifies the volume-limited sample used in each case. The star in samples 8 and 9 indicates the GAMA samples for which $H\alpha$ and $[N\text{II}]\lambda 6584$ are strongly affected by sky lines. The blue solid line, shown in all panels, corresponds to a second-order polynomial fit to the local SDSS and GAMA samples up to $z \sim 0.1$ (equation 7). The blue dashed lines indicate the 1σ dispersion for this fit. The green solid line shows the result of fitting the zero-point in equation (7) to each sample. The vertical dot–dashed lines correspond to the mass limits of SDSS (grey) and GAMA (red). The pink and purple circles correspond to the median metallicity in bins of stellar mass for SDSS and GAMA, respectively. The right-hand panels show the concatenated samples V1–V4, with their respective redshift range at the bottom of each panel. The yellow circles indicate the median metallicity in bins of stellar mass taking GAMA and SDSS galaxies as a single sample.

affected by sky lines. The metallicity and SFR for these SDSS samples, however, are not affected by sky line emission contamination because all emission lines were used to derive these values. Therefore, we only consider data from the SDSS survey in samples 8 and 9.

To improve our statistical reliability within the subsamples, and to measure the metallicity and SFR evolution more accurately, we concatenated samples with similar offsets in metallicity and SFR. Samples 1–4 form the sample V1; samples 5–8 (5–7 for GAMA) form sample V2; samples 9–12 (10–12 for GAMA) form sample V3; and samples 13–6 form sample V4. The new samples V1–V4 are shown in the right-hand panels of Figs 6–9. These samples will be used to analyse the dependences between M_* , SFR and Z (Section 5) and to study the FP (Section 4).

Since galaxies up to $z \sim 0.1$ do not show any sign of metallicity evolution in the M_* – Z relation and cover a wide range in stellar mass, we fit a second-order polynomial to sample V1. To get a robust fit, we are only considering galaxies between the mass limits

shown by the vertical lines, and given in Fig. 2. The local fit to the M_* – Z relation is given by

$$12 + \log(\text{O}/\text{H}) = -10.8297 + 3.6478x - 0.16706x^2, \quad (7)$$

where $x = \log(M_*/M_\odot)$ and $\sigma = 0.150$.

This local M_* – Z relation is plotted in all the 16 samples shown in Fig. 6. To measure metallicity evolution, we consider as a single sample all galaxies from both the SDSS and GAMA surveys, as shown in each panel of Fig. 6. Then, we fitted the zero-point of equation (7) for each sample. The resulting offset is shown by a green line in each panel of Fig. 6, and the difference between the local and fitted zero-point is given in Table 2. In the case of the concatenated samples V1–V4, the offset was also estimated taking into account both the GAMA and SDSS galaxies as a single sample.

From Fig. 6, it is evident that the metallicity decreases with increasing redshift. The highest difference between local and redshifted galaxies is found in sample 16 ($0.330 < z < 0.365$), which has an oxygen abundance that is ~ 0.139 dex lower than that

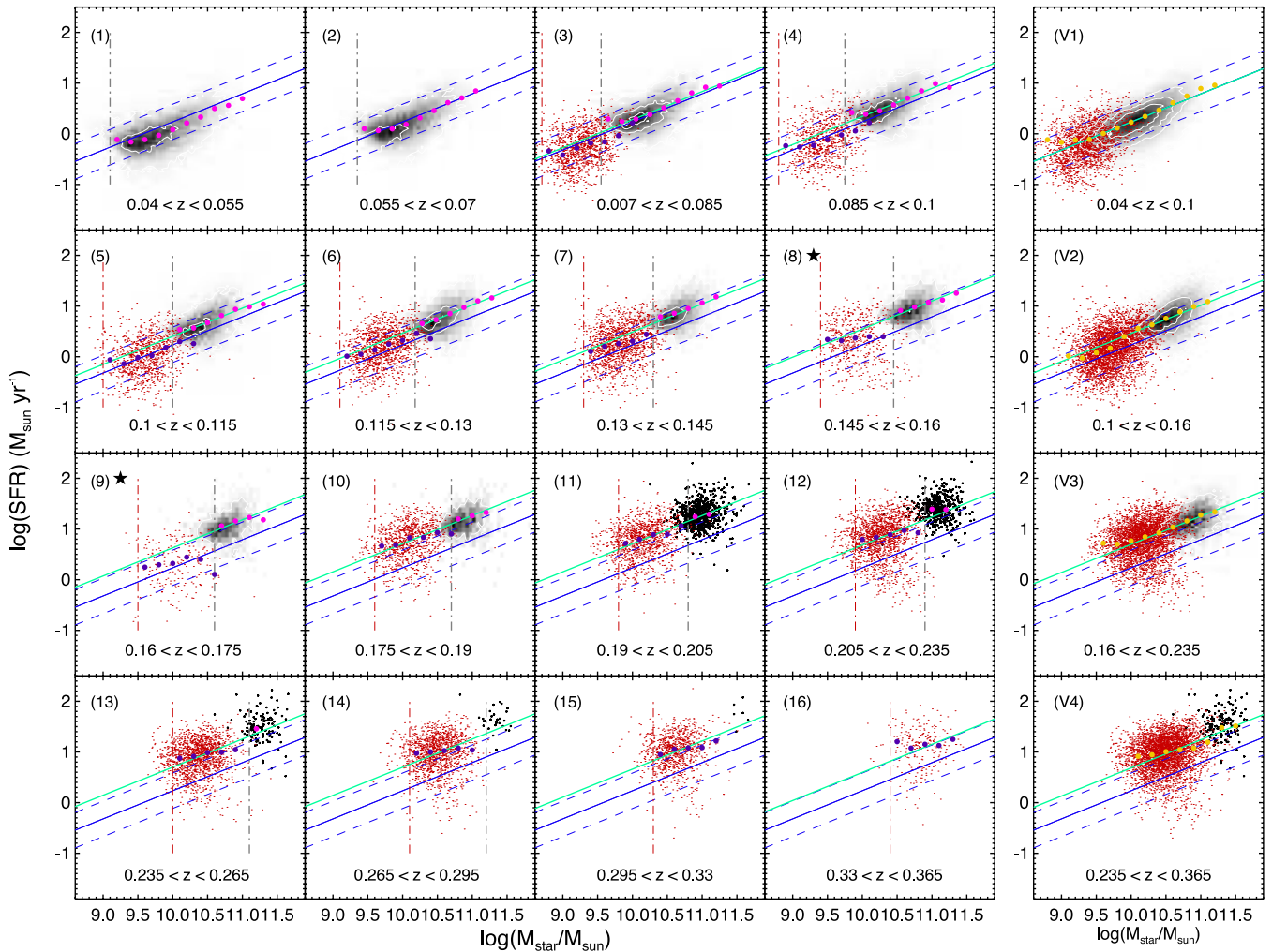


Figure 7. As in Fig. 6, but now showing the M_* –SFR relation. Symbols, annotations and lines are as in Fig. 6. The blue solid line, shown in all panels, corresponds to a linear fit to the local samples up to $z \sim 0.1$ (equation 8). The blue dashed lines indicate the 1σ dispersion for this fit. The green solid line shows the fit to the zero-point of the local relation. The pink and purple circles correspond to the median SFR in bins of stellar mass for SDSS, and GAMA, respectively. The yellow circles indicate the median SFR in bins of stellar mass taking GAMA and SDSS galaxies as a single sample.

observed in local galaxies. The median error in metallicity of the concatenated samples are 0.048, 0.047, 0.047 and 0.052 dex for samples V1, V2, V3 and V4, respectively. The median error is not only smaller than the possible evolution seen, but being a random error it is unlikely that the whole population would suffer a similar decrement randomly.

A metallicity evolution at redshifts $z \leq 0.4$ was also found by Lara-López et al. (2009a, 2009b) and Pilyugin & Thuan (2011). In both studies, the oxygen abundance shows a decline of up to ~ 0.1 dex between local and $z \sim 0.4$ galaxies. This metallicity evolution agrees with the predictions given by the models of Buat et al. (2008) for galaxies with a velocity dispersion of ~ 360 km s $^{-1}$ and $\log(M_*/M_\odot) \sim 11.25$.

In a similar way, we generated the M_* –SFR relation for all our samples. Fig. 7 shows this relation, which can be represented by a linear fit. The M_* –SFR relation for local galaxies up to $z \sim 0.1$ (sample V1) is given by

$$\log(\text{SFR}) = -5.3126 + 0.5547x, \quad (8)$$

where $x = \log(M_*/M_\odot)$ and $\sigma = 0.349$

As we did in the case of the M_* – Z relation, we fitted the zero-point of equation (8) for each volume-limited sample considering

all galaxy data from GAMA and SDSS as a single sample. The difference between the local and the fitted zero-point is listed in Table 2. As can be seen, the SFR evolves to higher values as redshift increases, with a median evolution up to $z = 0.365$ of ~ 0.4 dex for sample V4.

As discussed in Section 2.1.3, we consider a Balmer decrement of ~ 7.58 as an upper limit to the dust correction to avoid overestimating the SFR in GAMA galaxies. There will be some systems that do have such high obscurations, however, that we are overlooking as a consequence. As a result, the evolution found in $\log(\text{SFR})$ should be taken as a lower limit, in the event that some number of intrinsically high obscuration systems are being erroneously excluded. Considering a more relaxed limit of 10 to the Balmer decrement, the evolution found for $\log(\text{SFR})$ in samples 13, 14, 15 and 16 is 0.05, 0.06, 0.05 and 0.07 dex greater, respectively, than the values listed in Table 2.

We also analyse the M_* –SSFR relation because it offers an excellent way of studying the effect of galaxy downsizing. Fig. 8 shows the analysis of the M_* –SSFR relation. We find results consistent with earlier work of the M_* –SSFR (e.g. Noeske et al. 2007; Bauer et al. 2013). A linear fit gives a good representation of the M_* –SSFR relation for these samples of SF galaxies.

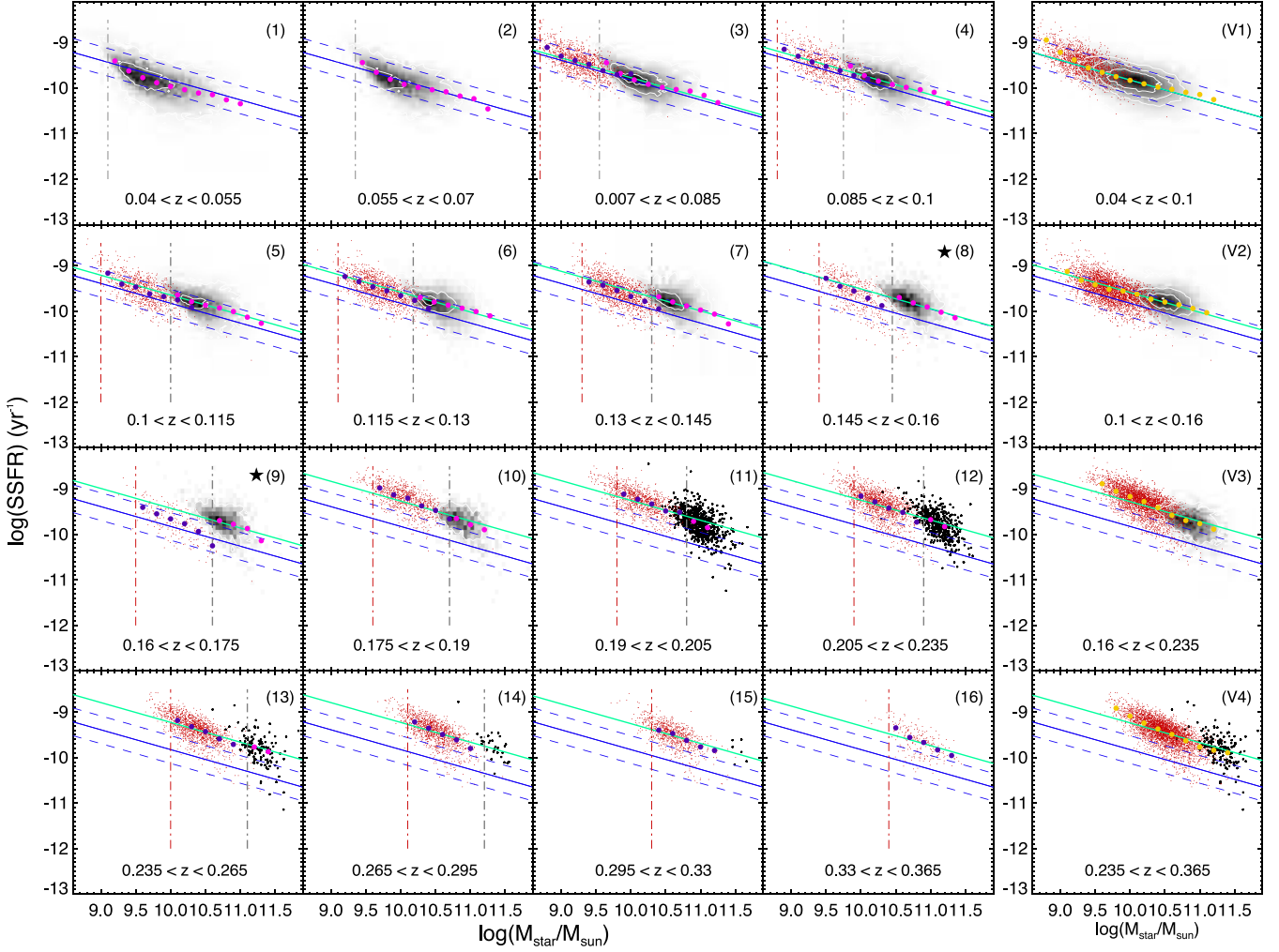


Figure 8. As in Fig. 6, but now showing the M_* –SSFR relation. The blue solid line, shown in all panels, corresponds to a linear fit to the local samples up to $z \sim 0.1$ (equation 9). The blue dashed lines indicate the 1σ dispersion for this fit. The green solid line shows the fit to the zero-point of the local relation. The yellow circles indicate the median SSFR in bins of stellar mass taking GAMA and SDSS galaxies as a single sample.

The M_* –SSFR relation for the local (sample V1, $z \lesssim 0.1$) is given by

$$\log(\text{SSFR}) = -5.479 - 0.434x, \quad (9)$$

where $x = \log(M_*/M_\odot)$ and $\sigma = 0.304$.

We again fit the zero-point of equation (9) for each volume-limited sample. The difference between the local and the fitted zero-point is listed in Table 2.

The high SSFR seen for low-mass galaxies indicates they are increasing their stellar mass, relatively speaking, more quickly than those at high mass (e.g. Noeske et al. 2007). We measure a change in the zero-point as large as the scatter in the relation over the $0 \lesssim z \lesssim 0.36$ span explored here. We find an evolution of 0.56 dex for sample V4 (see Table 2).

Finally, Fig. 9 studies the Z –SFR relation. As already discussed, this relation has the broadest scatter of all combinations of SFR, M_* and Z . A third-order polynomial fit to the V1 sample yields

$$\log(\text{SFR}) = -1443.97 + 508.48x - 59.692x^2 + 2.336x^3, \quad (10)$$

where $x = 12 + \log(\text{O}/\text{H})$ and $\sigma = 0.2$. Since this relation has a very high dispersion and both variables, Z and SFR, evolve with redshift, we do not measure any evolution in this relationship. However, we

observe a general tendency for the SFR to increase with metallicity for all the volume limited samples. We discuss the Z –SFR relation in detail in Section 5.

4 THE FUNDAMENTAL PLANE

We generate the FP considering all the volume-limited samples for the GAMA and SDSS galaxies as a single sample. The M_* – Z , M_* –SFR and Z –SFR relationships are the projections of this 3D distribution. While M_* correlates with both SFR and metallicity (the well-known M_* – Z and M_* –SFR relationships), the SFR does not strongly correlate with metallicity (see Fig. 9), which means that this relation is close to the face-on view of the 3D distribution (see top-left panel of Fig. 10).

Lara-López et al. (2013b) explore different methods to analyse and give the best representation to the M_* – Z –SFR space. The methods analysed include principal component analysis (PCA), regression and binning data. The result that best quantifies the distribution of galaxy measurements in this space is by fitting a plane to the stellar mass using regression. Although PCA does not give the best fit, a PCA analysis for our GAMA and SDSS sample indicates that the first two principal components account for

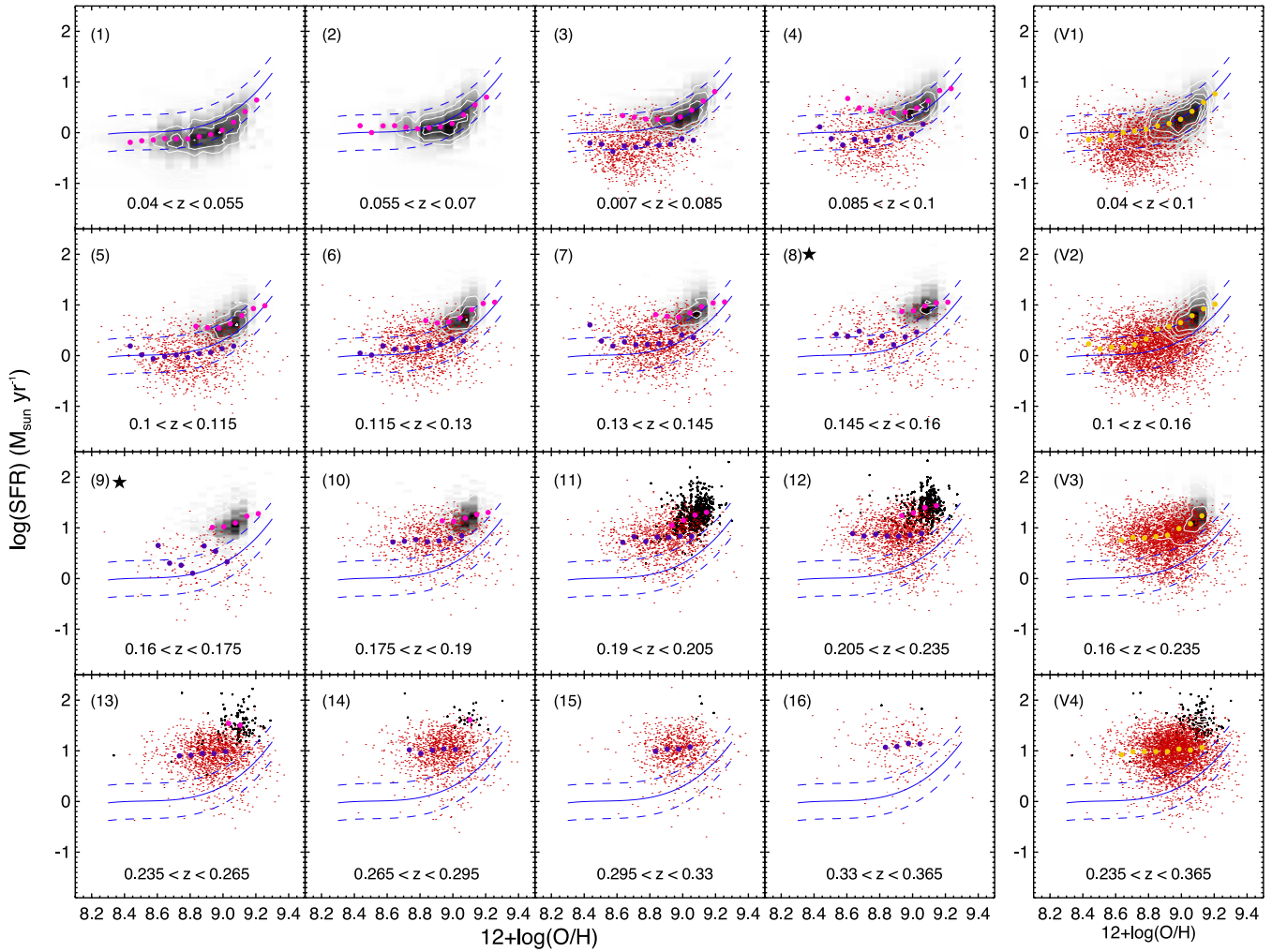


Figure 9. As in Fig. 6, but now showing the Z-SFR relation. The blue solid line, shown in all panels, corresponds to a third-order polynomial fit to the local samples up to $z \sim 0.1$ (equation 10). The blue dashed lines indicate the 1σ dispersion for this fit. The yellow circles indicate the median SFR in bins of Z taking GAMA and SDSS galaxies as a single sample.

Table 2. Evolution found in $12+\log(\text{O}/\text{H})$, SFR and SSFR for the 16 volume-limited samples, and four concatenated samples.

| Sample | Redshift range | Evolution (dex) | | | | | |
|--------|----------------|------------------------------|--------------------|---------------------|----------|-------|----------|
| | | $12+\log(\text{O}/\text{H})$ | $\log(\text{SFR})$ | $\log(\text{SSFR})$ | | | |
| 1 | 0.04:0.055 | – | – | – | – | | |
| 2 | 0.055:0.07 | – | V1:– | V1:– | V1:– | | |
| 3 | 0.070:0.085 | – | – | – | – | | |
| 4 | 0.085:0.1 | – | – | – | – | | |
| 5 | 0.1:0.115 | 0.011 | 0.168 | 0.180 | | | |
| 6 | 0.115:0.130 | 0.016 | V2:0.016 | 0.231 | V2:.225 | 0.240 | V2:0.234 |
| 7 | 0.130:0.145 | 0.022 | – | 0.252 | – | 0.266 | – |
| 8 | 0.145:0.160 | 0.021 | – | 0.310 | – | 0.314 | – |
| 9 | 0.160:0.175 | 0.035 | – | 0.392 | – | 0.398 | – |
| 10 | 0.175:0.190 | 0.034 | V3:0.049 | 0.472 | V3:0.459 | 0.552 | V3:0.542 |
| 11 | 0.190:0.205 | 0.058 | – | 0.471 | – | 0.567 | – |
| 12 | 0.205:0.235 | 0.066 | – | 0.443 | – | 0.571 | – |
| 13 | 0.235:0.265 | 0.077 | – | 0.459 | – | 0.592 | – |
| 14 | 0.265:0.295 | 0.093 | V4:0.088 | 0.456 | V4:0.444 | 0.591 | V4:0.581 |
| 15 | 0.295:0.330 | 0.083 | – | 0.419 | – | 0.564 | – |
| 16 | 0.330:0.365 | 0.15 | – | 0.354 | – | 0.516 | – |

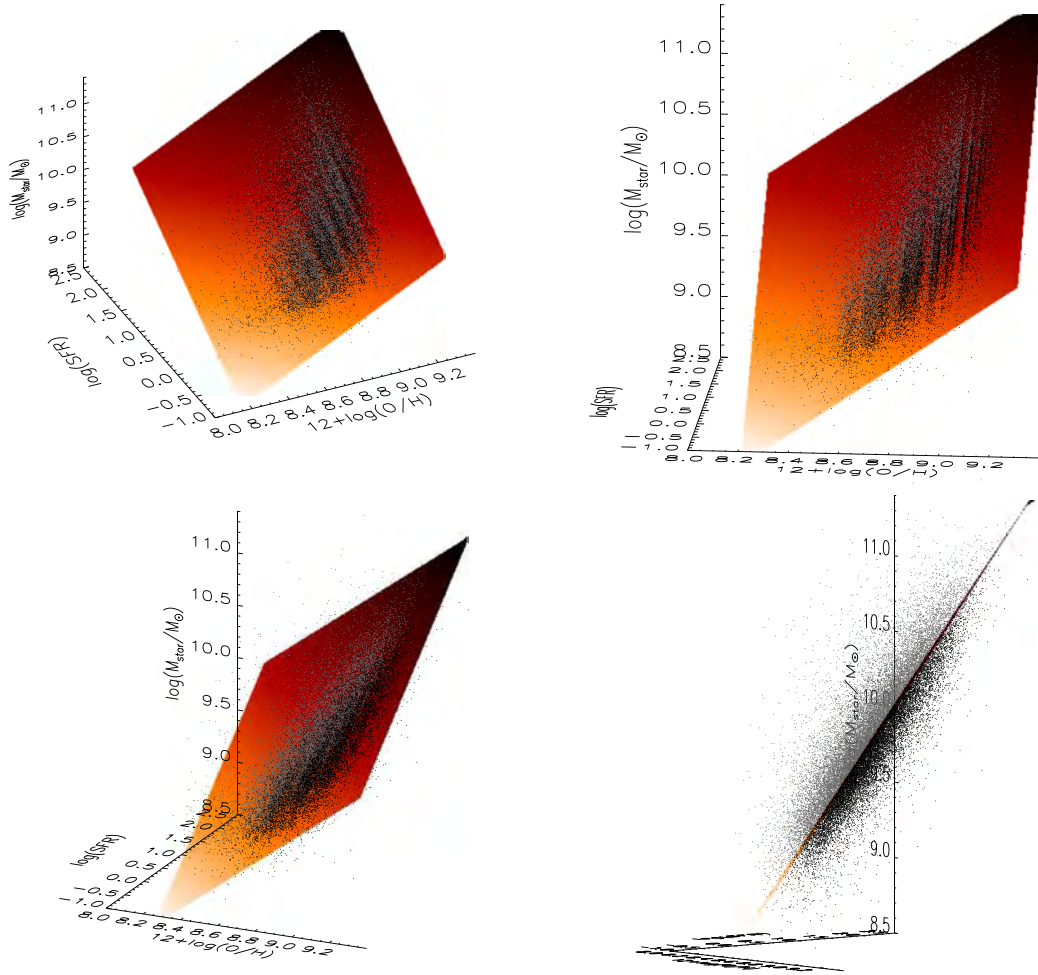


Figure 10. Projections of the 3D distribution formed by M_* , $\log(\text{SFR})$ and $12+\log(\text{O}/\text{H})$ for GAMA and SDSS galaxies. The orange plane shows the FP described in equation (11). The vertical axis shows M_* in all panels. The cube is rotated clockwise from the upper-left to the bottom-right panel. This last panel shows the edge-on projection of our derived FP. The grey and black dots show galaxies above and below the FP, respectively.

98 per cent of the variance, confirming that a planar representation is appropriate.

Following Lara-López et al. (2010b) and Lara-López et al. (2013b), we fitted a plane to M_* using regression:

$$\log(M_*/M_\odot) = \alpha [12 + \log(\text{O}/\text{H})] + \beta [\log(\text{SFR})] + \gamma, \quad (11)$$

where $\alpha = 1.3764 \pm 0.006$, $\beta = 0.6073 \pm 0.002$ and $\gamma = -2.5499 \pm 0.058$. The FP given by equation (11), which provides a good approximation to our data, is shown in Figs 10 and 11. This relation recovers the M_* of our entire sample with $\sigma = 0.2$ dex. As demonstrated by Lara-López et al. (2010b), this FP can also recover the M_* of high-redshift galaxies, and shows a lack of evolution up to $z \sim 3.5$. See Lara-López et al. (2010b) for a detailed discussion.

The FP is a consequence of the tight dependence of M_* on SFR and Z . The current mass locked up in stars in a galaxy (M_*) is a measure of the amount of gas currently being converted into stars (SFR), plus a measure of the star formation history, or past generations of stars, here represented by the metallicity (Z). So in broad terms, the value of M_* can be thought of as being dependent on a combination of the current SFR and the star formation history of a galaxy.

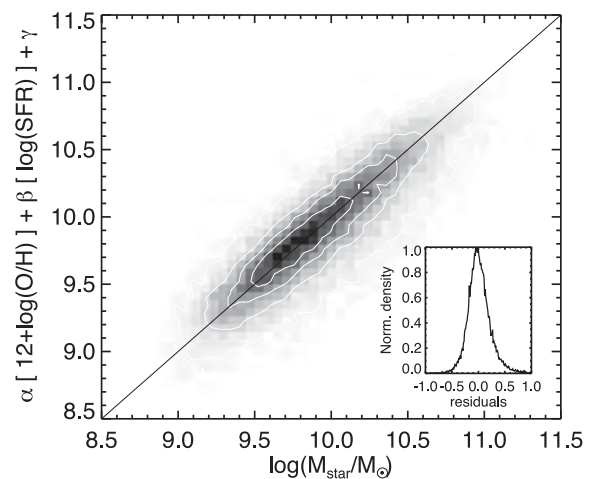


Figure 11. Projection of the FP for the GAMA and SDSS galaxies. The horizontal axis shows the observed M_* , while the vertical axis shows the M_* estimated through the FP described in equation (11). The enclosed panel shows the histogram of the residuals with $\sigma = 0.2$ dex.

To explain the lack of evolution in the FP, a description of how galaxies evolve is needed. At high redshifts, (proto-)galaxies are characterized by stars of first generation that have not yet processed their gas. This implies low gas metallicities and very high SFRs and SSFRs. However, galaxies in the local universe are characterized for stars of later generations that have been formed from pre-enriched gas and reached higher gas metallicities. As these galaxies have a large amount of gas locked up into stars they show a lower SFR than those galaxies observed in the primitive universe. Hence, there is an equilibrium between Z and SFR at all redshifts. At high redshifts, the SFR is the fundamental parameter that drives the evolution of the galaxies. In the local universe, however, Z is the dominant parameter as the result of the gas processed into stars. SFR and Z are evolving in opposite directions: while high-redshift galaxies show high SFRs and low Z , low-redshift galaxies host low SFRs and high metallicities. Hence, a linear combination of Z and SFR will tend to cancel out evolution of the FP with redshift. The evolution of the FP was studied by Lara-López et al. (2010b), who show that it does not evolve up to $z \sim 3.5$.

It is noteworthy that although we are finding evolution in Z and SFR as redshift increases, this is not in contradiction with the absence of evolution found in the FP. The FP suggests a new way of interpreting the stellar mass as a dependent property of both, Z and SFR. The fact that the same FP can be used to recover the stellar mass of a galaxy at high redshift is a consequence of the evolution in opposite directions of the Z and SFR, as mentioned above.

5 SFR, SSFR, METALLICITY AND STELLAR MASS DEPENDENCES

To understand the properties of a pair of variables as a function of a third one, we perform a 2D analysis of the four variables we have been working on. For the volume-limited samples V1–V4, taking into account both SDSS and GAMA galaxies as a single sample, we study the SFR and SSFR dependence on the M_* – Z relation, the Z dependence on the M_* –SFR and M_* –SSFR relations, and the M_* dependence on the Z –SFR and Z –SSFR relations (see Figs 12–15).

For these relationships, we can use the median values of one variable within bins of the other two to look at overall trends. When doing this, however, care must be taken to correctly interpret the results. For example, when studying the SFR dependence of the M_* – Z relation, we obtain results that at first glance appear different if we estimate the median M_* in bins of metallicity (vertical bins, see Fig. 13a), or the median Z in bins of stellar mass (horizontal bins, see Fig. 12a). These results are not contradictory, but provide different information. They should be carefully interpreted as saying, in the former case, how the median *stellar mass* varies for a given SFR and metallicity, and in the latter how the median *metallicity* varies for a given SFR and stellar mass. These are clearly not the same thing, although in a diagram such as this it is easy to confuse the interpretation. To disentangle the different information that each binning direction provides, we analyse both.

Figs 12 and 14 show the combinations of the different dependences of M_* , Z , SFR and SSFR. In these figures, we take bins of the horizontal variable and estimate the median value of the vertical variable in bins of the third. Figs 13 and 15 show exactly the same distributions, but now binning in the other direction. Here, we perform the binning in the vertical variable and estimate the median value of the horizontal variable in bins of the third. In each panel, the vertical and horizontal colour lines show the 1σ dispersion of four representative bins of the variable shown in the colour bar.

5.1 Horizontal bins: estimating Z , SFR and SSFR

Fig. 12(a) shows the M_* – Z relation taking Z as the principal variable to determine, the median Z in bins of M_* and SFR. We see a reversal at $\log(M/M_\odot) \sim 10.2$ in the SFR dependence of the metallicity of galaxies. For $\log(M/M_\odot) \gtrsim 10.2$, galaxies with high SFRs have higher metallicities than galaxies with lower SFRs. On the contrary, for $\log(M/M_\odot) \lesssim 10.2$, galaxies with high SFRs show lower metallicities than galaxies with lower SFRs. As redshift increases, we still observe the same tendency for samples V2 to V3, and although the sample V4 does not span a broad range of M_* , our data suggest a similar trend. Sample V4 shows the metallicity evolution discussed in the previous section. Galaxies with a high SFR (pink circles in Fig 12a) have metallicities which are ~ 0.07 dex lower than that observed in sample V1. Considering the SSFR dependence (Fig. 12b), a similar behaviour is found for $\log(M/M_\odot) \lesssim 10.2$, in the sense that galaxies with higher SSFR have lower metallicities than galaxies with a lower SSFR, and vice versa for higher mass systems.

Figs 12(c) and (d) show the M_* –SFR and M_* –SSFR relationships taking the median SFR (and SSFR) in bins of M_* and Z . In this case, we observe again the same reversal shown in for Figs 12(a) and (b). At the high-mass end of the M_* –SFR (–SSFR) relation, galaxies with high metallicity show higher SFR (and SSFR) than galaxies with lower metallicity. On the other hand, at the low-mass end of the M_* –SFR (SSFR) relation, galaxies with a high metallicity show lower SFR (and SSFR) than low-metallicity galaxies.

To explain this behaviour, imagine two galaxies at the same redshift with similar stellar masses ($\log(M/M_\odot) \sim 11 M_\odot$), but one with a higher amount of neutral gas than the other. Since both galaxies are massive, downsizing indicates that they are going to process their gas quickly. Then, the galaxy with a larger amount of gas will reach higher metallicities and will have a higher SFR and SSFR than the galaxy with less neutral gas.

On the other hand, we now consider two low-mass galaxies ($\log(M/M_\odot) \sim 9.5 M_\odot$) but one hosting more neutral gas than the other. Downsizing indicates that, due to their low stellar mass, both galaxies will process their gas slowly and on longer time-scales than massive galaxies. According to Fig. 12(b), low-mass galaxies with a high SSFR show lower metallicities than galaxies with a lower SSFR. The high metallicity of low-mass galaxies can be explained for a more bursty star formation in the past that exhausted its gas and increased its metallicity.

From these considerations, we infer that both the amount of baryonic mass (stars plus gas) and downsizing are driving the rate at which a galaxy is producing their metals. Massive galaxies with a large amount of gas will process their gas faster and reach higher metallicities than a similar galaxy with a smaller amount gas. A low-mass galaxy with a large amount of gas, however, will tend to have a very low star formation efficiency, resulting in lower metallicities than a similar galaxy with lower gas, which have experimented a bursty star formation in the past. A detailed model of this picture is given in Lara-López et al. (2013a).

5.2 Vertical bins: estimating M_*

Now we consider stellar mass as the principal variable to be determined as a function of the others. Fig. 13(a) shows the M_* – Z relation derived taking the median M_* in bins of Z and SFR. The median values in this relation show that at a given metallicity, galaxies with higher SFR have higher median M_* .

It is possible to project the FP over the M_* – Z face of the 3D-cube by giving values to the SFR and Z and then estimate the M_* through

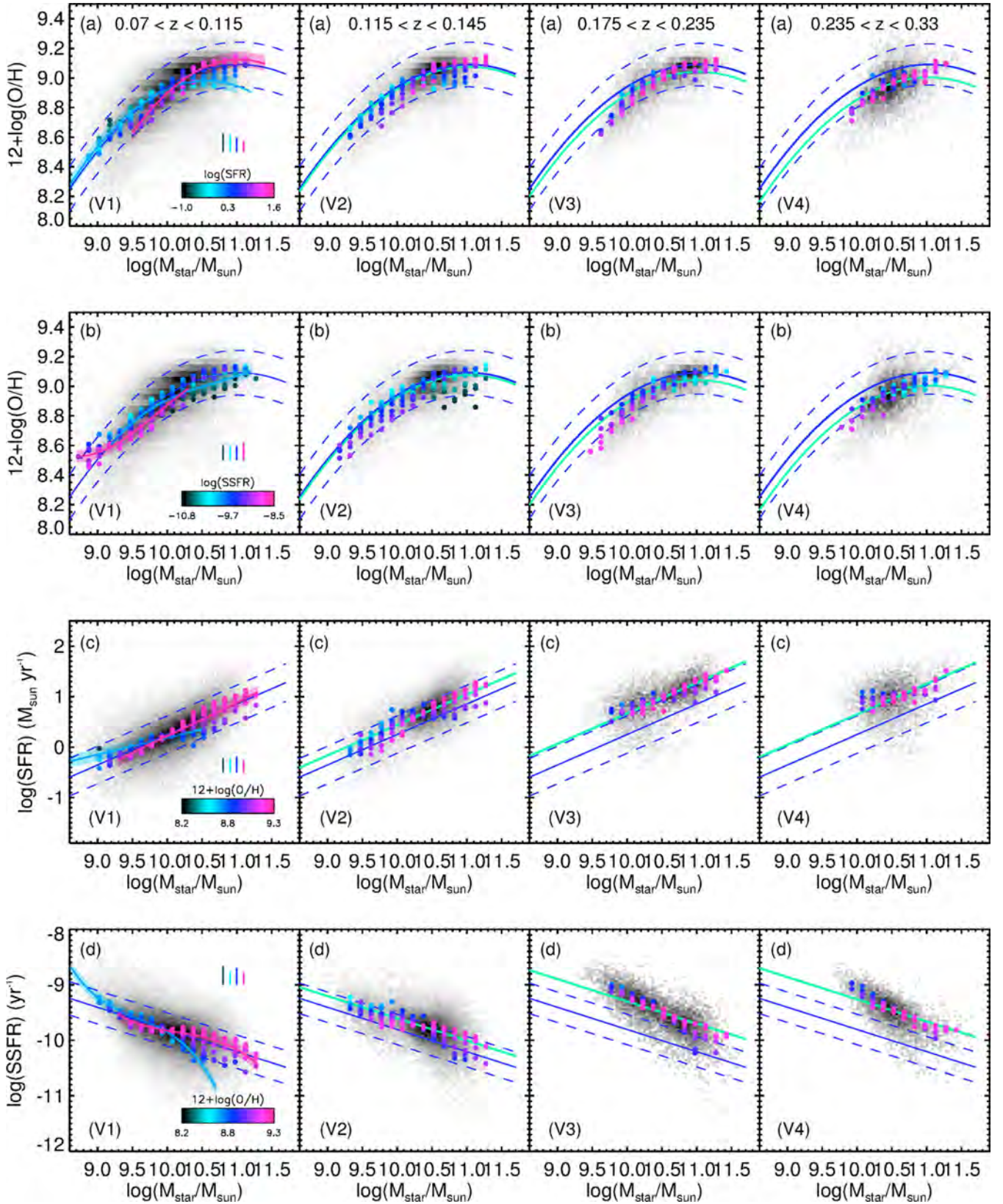


Figure 12. From top to bottom, the SFR dependence of the M_* – Z relation, the SSFR dependence of the M_* – Z relation, the Z dependence of the M_* –SFR relation and the Z dependence of the M_* –SSFR relation. In all panels, we show the median value of the vertical variable in M_* bins (horizontal bins) for every bin of the third variable. The pink and blue ribbons in the left-hand panels highlight the median circles of the high- and low-mass end, respectively. The vertical colour lines show the 1σ dispersion of the vertical variable of four representative bins, as shown in the colour-bar of each panel. The data density corresponds to the SDSS and GAMA sample together.

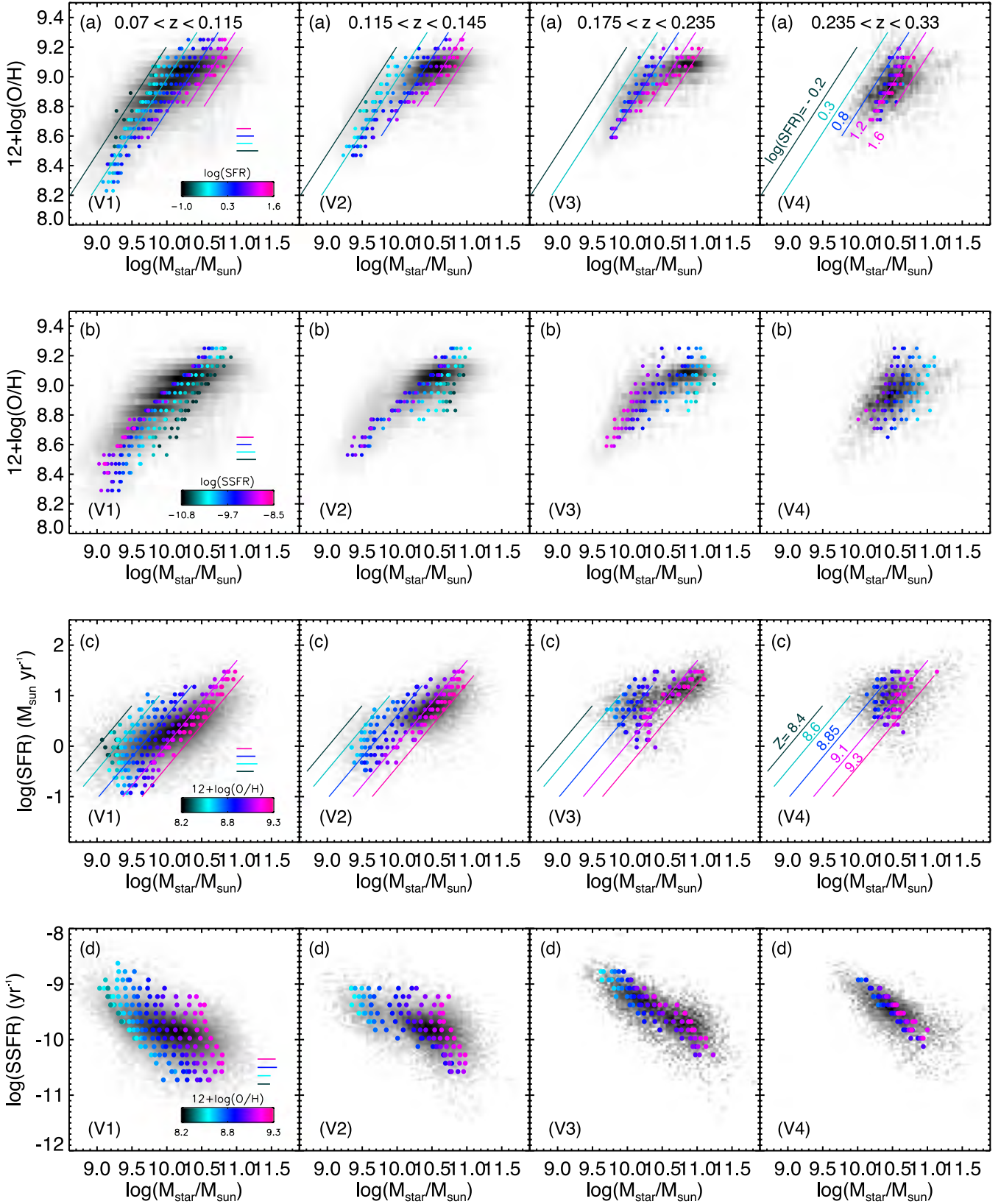


Figure 13. From top to bottom, the SFR dependence of the $M_* - Z$ relation, the SSFR dependence of the $M_* - Z$ relation, the Z dependence of the $M_* - \text{SFR}$ relation and the Z dependence of the $M_* - \text{SSFR}$ relation. In all panels, we show the median M_* in bins of the vertical variable (vertical bins) for every bin of the third variable. The horizontal colour lines show the 1σ dispersion of the horizontal variable of four representative bins, as shown in the colour-bar of each panel. The data density grey-scale corresponds to the SDSS and GAMA sample together.

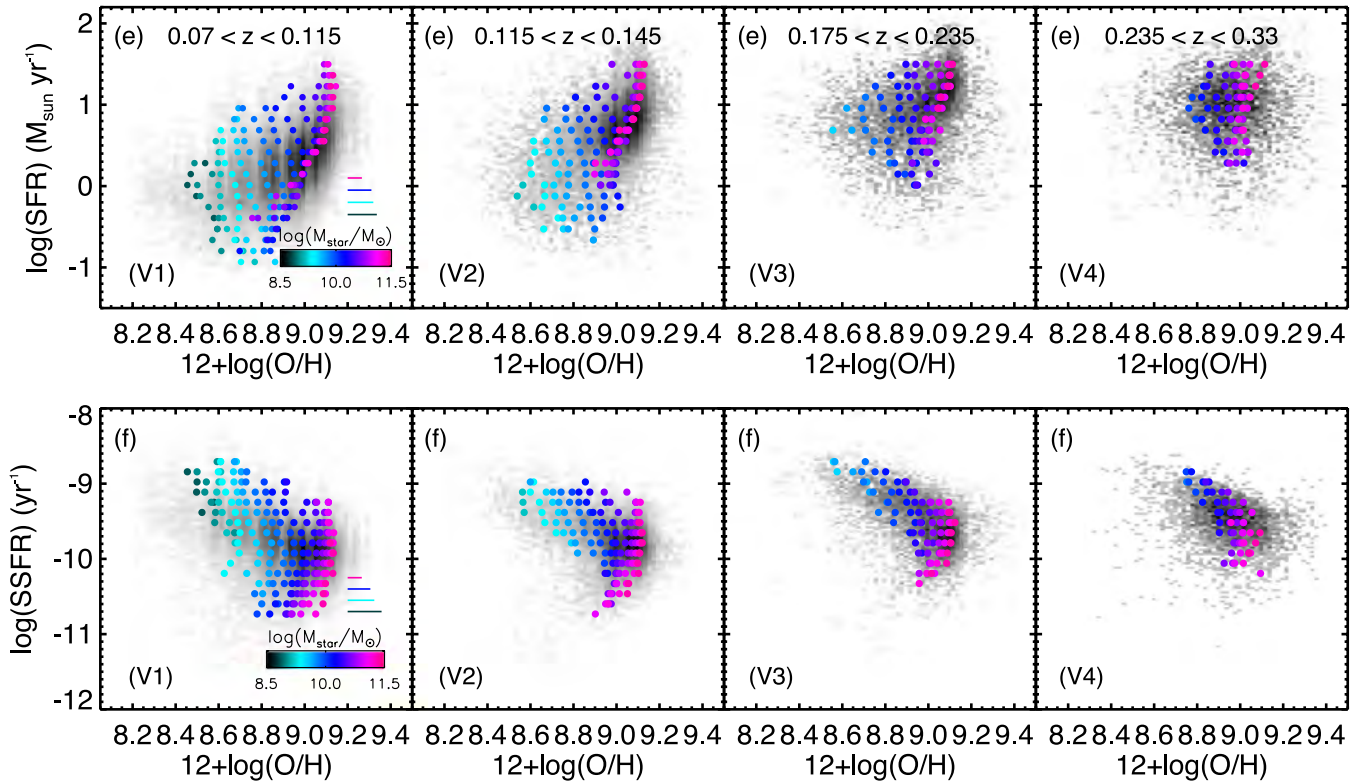


Figure 14. From top to bottom, the M_* dependence of the Z-SFR and Z-SSFR relations. The median metallicity in bins of SFR and SSFR for given bins of M_* is shown in all cases. The horizontal colour lines show the 1σ dispersion of the horizontal variable of four representative bins, as shown in the colour-bar of each panel. The data density grey-scale corresponds to the SDSS and GAMA sample together.

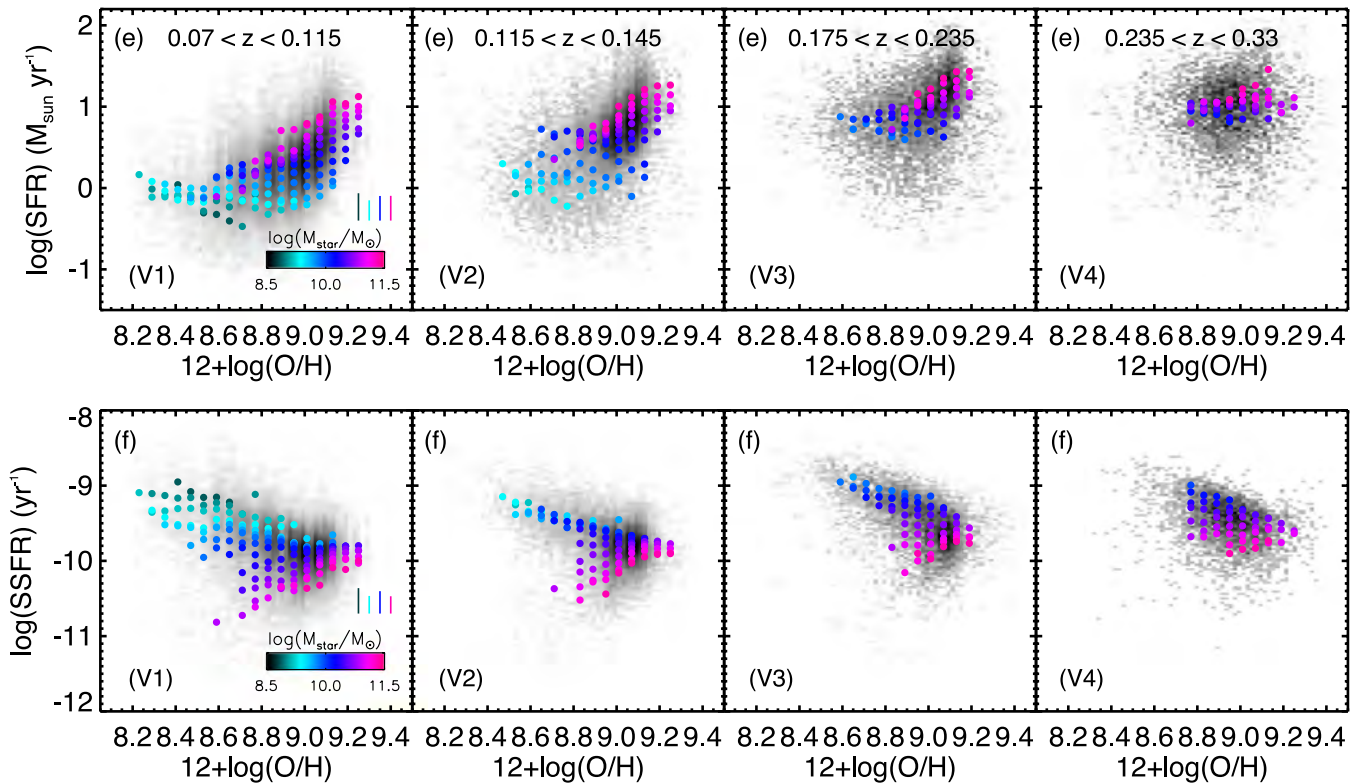


Figure 15. From top to bottom, the M_* dependence of the Z-SFR and Z-SSFR relation. The median SFR and SSFR in bins of metallicity for different bins of M_* is plotted in all cases. The vertical colour lines show the 1σ dispersion of the vertical variable of four representative bins, as shown in the colour-bar of each panel. The grey density plot correspond to the SDSS and GAMA sample together.

equation (11). Following this procedure, we obtain the projections of the FP shown in Fig. 13(a), which matches the median M_* values found before.

Since the SSFR is a more physical quantity showing the actual amount of stars formed per unit mass, we show the SSFR versus Z in Fig. 13(b). In this case, we see that low-mass galaxies have low Z and high SSFR. Indeed, at any Z , higher SSFR galaxies are seen to have lower mass than those with lower SSFR.

Fig. 13(c) shows the M_* -SFR relation as a function of metallicity taking the median M_* in bins of SFR and Z . For a given SFR, higher metallicity systems have higher stellar mass, i.e. we are obtaining the M_* - Z relation. The solid lines in Fig. 13(c) show the projection of the FP over this M_* -SFR relation and confirm that, at fixed metallicity, the median M_* is higher for higher SFR.

Finally, Fig. 13(d) studies the M_* -SSFR relation as a function of metallicity. Again, at a given SSFR, higher metallicity galaxies have higher median stellar mass. Similarly, at a given metallicity, higher SSFR systems have lower median stellar mass.

Together, all these approaches to exploring the distribution of M_* , SFR and Z provide a consistent picture of galaxy properties. In particular, the reversal seen in Fig. 12 in the dependence of Z on SFR or SSFR as a function of mass is tantalizingly suggestive of a key role being played by the gas reservoir available for forming stars.

Any evolution of the Z or SFR will be along the projection of the plane. For example, sample V4 of Fig. 13(a) shows an evolution towards lower values of Z . However, this evolution actually comes from the projections of the FP on the M_* - Z relation. On the other hand, sample V4 of Fig. 13(c) shows an SFR evolution towards higher values of SFR. This evolution is again happening along the projections of the FP.

Finally, we examine the typical dispersions of vertical and horizontal bins in the M_* - Z relation. In order to compare the degree of dispersion of two different variables, we use the coefficient of variation $C_v \equiv \sigma/\mu$, where σ is the standard deviation and μ is the mean. We estimate the coefficient of variation for all our median values of Figs 12(a) and 13(a), obtaining a typical $C_v = 0.01$ for the metallicity median points, and $C_v = 0.02$ for the M_* median points. This means that the degree of variation around the median points of metallicity is of the order of 1 per cent, and 2 per cent for the M_* median points, allowing us to infer the physical dependences through both representations.

5.3 Some special cases: the Z -SFR and Z -SSFR relations

Although the dependences previously shown exhibit different median values depending on the assumed binning direction, the general tendencies are similar (e.g. Z and SFR always increase with M_*). However, the Z -SFR and Z -SSFR relations are special cases because they have a high scatter, and hence the median values drastically change depending on the binning direction taken, and care must be taken when interpreting the data.

Fig. 14(e) shows how the median metallicity varies in bins of SFR and M_* . The median metallicity of galaxies increases as SFR increases for high-mass galaxies, but decreases as SFR increases for low-mass galaxies. Following the same model described in Section 5.1, these changes can be attributed to different gas content in galaxies at different stellar masses.

On the other hand, Fig. 15(e) shows the same relation as Fig. 14(e) but now considering the median SFR in bins of Z and M_* . The median SFR values indicate that SFR increases when metallicity increases for massive galaxies. For low-mass galaxies, however, the

SFR remains almost constant, or slightly decreasing when metallicity increases. Therefore, independently of the binning direction taken, the result drives us to similar conclusions.

Fig. 14(f) shows the Z -SSFR relation taking the median Z in bins of SSFR and M_* . In this case, a reverse is observed around $\log(\text{SSFR}) \sim -10$. For $\log(\text{SSFR}) \gtrsim -10$, the Z of galaxies decreases when the SSFR increases, and vice versa for $\log(\text{SSFR}) \lesssim -10$. The same tendency is observed in the high-redshift samples. This reverse is the same observed in Fig. 12(d), and agrees with the hypothesis of a different amount of gas for different stellar masses. This reverse is more evident in Fig. 15(f), that shows the same relationship but taking the median SSFR in bins of Z and M_* . Interestingly, the median SSFR values show two tails: one formed by low-mass galaxies displaying high SSFRs, in which the SSFR anticorrelates with Z , and another formed by massive galaxies with low SSFRs, in which the SSFR correlates with Z . Both tails converge to a $\log(\text{SSFR})$ value of ~ -10 .

This dual behaviour is a consequence of the different physics involving low- and high-mass galaxies. The same explanation given in Section 5.1 is applicable here. A combination of both downsizing, and the differences in the amount of neutral gas in galaxies can explain the bimodality observed in those relationships. For low- and high-mass galaxies, galaxies with a higher amount of gas will show higher SSFRs compared to galaxies at the same mass but with less H I.

Our explanation agrees with Davé, Finlator & Oppenheimer (2012), who through an analytic formalism inspired by hydrodynamic simulations describe an equilibrium between metallicity, gas fraction and SFR. According to their predictions, at a given mass, galaxies that are gas rich and metal poor will have higher SFRs. On the other hand, gas-poor and metal-rich galaxies will have lower SFRs.

The high-mass branch shown as pink points in Fig. 15(f) shows a positive correlation between Z and SSFR. Lara-López et al. (2013a) find that the amount of massive galaxies with H I detected is too few to confirm the proposed physical explanation. It is also possible, however, that AGN feedback could be implicated in shutting down the SFR in massive galaxies. It is likely that the effectiveness of this process varies from one massive galaxy to another, probably depending on the history of its AGN activity. One could then imagine that the systems in which star formation was shut down earliest would have especially low SSFR and also low average metallicity, since there has been less opportunity for metals to be recycled into subsequent generations of stars. Galaxies which have experienced less efficient AGN feedback would be left with more gas, but will also have had more opportunity to recycle it, increasing their metallicity.

As shown in Section 2, most of the objects in our sample correspond to late-type galaxies. Nevertheless, we studied the same relationships as a function of their Sérsic index to explore another possible explanation of this reverse as a function of morphology. However, we did not find any dependence with the Sérsic index. Thus, this opposite behaviour between low- and high-mass galaxies seems likely to be explained primarily by the different amount of gas in each. A more detailed explanation of this model is given in Lara-López et al. (2013a).

5.4 Dependences using different metallicities and SFR indicators

Here, we analyse how strongly the M_* - Z relation depends on several tracers of SFR and metallicity. We use only our SDSS

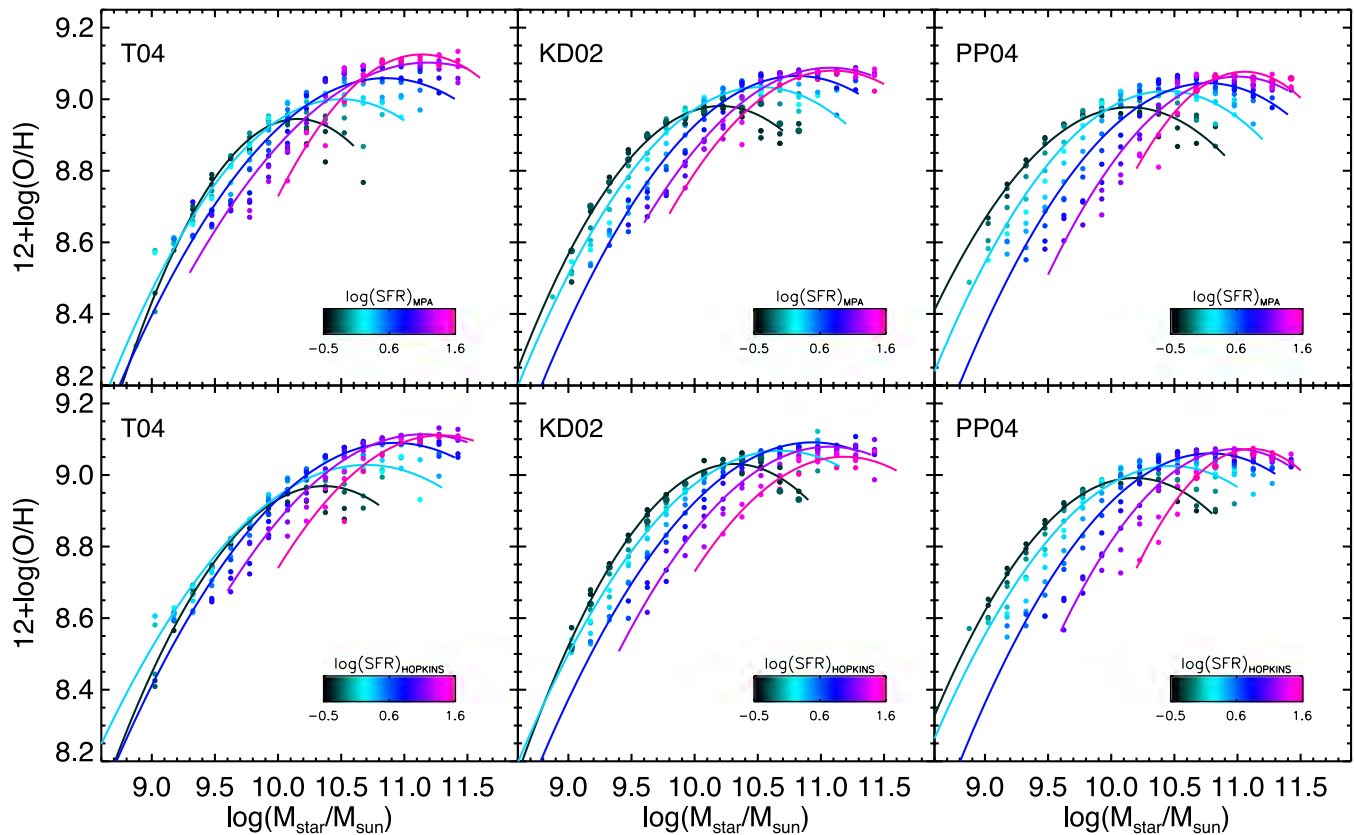


Figure 16. M_* – Z relation for SDSS galaxies up to $z < 0.365$. Left-hand column shows the M_* – Z relation using the Tremonti et al. (2004) metallicities and the Brinchmann et al. (2004) and Hopkins et al. (2003) SFRs. Middle and right-hand columns show the same relation but using the Kewley & Dopita (2002) and the Pettini & Pagel (2004) metallicities, respectively, with the same SFRs described above.

volume-limited galaxy samples, and adopt the following three different methods to estimate metallicities:

- (i) the Tremonti et al. (2004) Bayesian metallicities,
- (ii) the $[\text{N II}]/[\text{O II}]$ index with the calibration provided by Kewley & Dopita (2002) and the update given by Kewley & Ellison (2008) and
- (iii) the O3N2 index, defined in equation (1), with the calibration of Pettini & Pagel (2004).

For estimating the SFR we used the same two methods described in Section 2.1.2,

- (i) the Brinchmann et al. (2004) Bayesian SFRs and
- (ii) the Hopkins et al. (2003) estimations of the SFRs, which are based on the EW of $\text{H}\alpha$.

Fig. 16 shows the SFR dependence on the M_* – Z relation considering all the possible combinations of the metallicity and SFR methods described above. Although the dependences vary somewhat from one combination to another, they all are observed in all these six combinations. It is noteworthy that the main change in the dependences are due to the approach used in estimating the metallicities and not the SFRs. This is consistent with recent work by Zahid et al. (2013) who find that the characteristic shape observed in Fig. 16 is related to the level of dust extinction.

Mannucci et al. (2010) reported a different SFR dependence on the M_* – Z relation. Following these authors, all the SFR median points seem to converge at the high-mass end. We attribute this behaviour to the use of the N2 method (which relies on the

$[\text{N II}]\lambda 6584/\text{H}\alpha$ ratio; see Pettini & Pagel 2004) for galaxies in the high-metallicity regime. It is well known that the N2 parameter is not useful for $12+\log(\text{O}/\text{H}) > 8.8$ (e.g. Yin et al. 2007; López-Sánchez et al. 2012), as at high metallicities the $[\text{N II}]\lambda 6584$ saturates and it is no longer an appropriate tracer of the oxygen abundance. As a result of using a non-robust metallicity indicator, the high-metallicity regime of Mannucci et al. (2010) is saturated, and hence the dependency with SFR is lost, showing an artificial convergence of SFR at high metallicities. See Lara-López et al. (2013b) for a detailed explanation of this issue.

6 SUMMARY AND CONCLUSIONS

We studied the M_* , Z , SFR and SSFR dependences and evolution, as well as the FP using SF galaxies of the GAMA and SDSS surveys. We find good agreement between the GAMA and SDSS survey in all cases. Indeed, both surveys compliment each other. We divided our whole sample in 16 volume-limited samples from redshift $z = 0.04$ to $z = 0.365$. Our findings can be summarized as follows.

- (i) From a statistically robust sample combining the GAMA and SDSS surveys in volume-limited samples up to $z < 0.1$, we established a local M_* – Z relation. By fitting the zero-point of the local M_* – Z relation, we quantified the metallicity evolution of every volume-limited sample, finding a gradual decrement of metallicity as redshift increases, with a maximum evolution of ~ 0.1 dex for the redshift range $0.330 < z < 0.365$. The evolution found is in agreement with the evolutionary models of Buat et al. (2008).

(ii) We studied the M_* -SFR and M_* -SSFR relationships as well. In a similar way as the M_* - Z relation, we established a local M_* -SFR (-SSFR) relation, and fitted the zero-point for all the volume-limited samples at higher redshift. We found a maximum SFR evolution of ~ 0.4 dex, and of ~ 0.56 dex in SSFR.

(iii) We analysed the FP for the whole GAMA and SDSS galaxies, finding good agreement between both samples and a single plane for both of them. The FP found allows us to recover the M_* of SF galaxies through a linear combination of SFR and Z with a $\sigma = 0.2$ dex. The FP is a consequence of the direct dependence of the M_* on the SFR and Z . The current mass in stars in a galaxy (M_*) is a measure of the amount of gas currently being converted into stars (SFR), plus a measure of the star formation history, or past generations of stars, here represented by the metallicity (Z).

(iv) No evidence of evolution has been shown in the FP in our sample ($z < 0.365$), and there is a lack of evolution up to $z \sim 3.5$ (see Lara-López et al. 2010b for details). This lack of evolution is a consequence of the SFR and Z evolving in different directions. While the SFR increases for high-redshift galaxies, Z decreases. Thus, when the linear combination to produce the FP is applied, those differences cancel out, allowing us to recover the M_* of the galaxies.

(v) We studied the dependences and relationships of the M_* , Z , SFR and SSFR, analysing all the possible combinations and binning directions. We studied the SFR and SSFR dependence on the M_* - Z relation, the Z dependence on the M_* -SFR and M_* -SSFR relations, and the M_* dependence on the Z -SFR and Z -SSFR relationships. All of them showing a strong dependence and correlations to each variable.

(vi) We found that a correct interpretation is crucial when different binning directions are studied. For example, the SFR dependence in the M_* - Z relation apparently changes either if we estimate the median Z in M_* and SFR bins (Fig. 12), or the median M_* in Z and SFR bins (Fig. 13). Nevertheless, the underlying physics is consistent with a single interpretation.

(vii) We found evidence of a reverse in the dependences of low- and high-mass galaxies. For massive galaxies, the median metallicity is higher/lower for high/low SFR galaxies at the same stellar mass. On the other hand, for low-mass galaxies we find the opposite behaviour, the median metallicity is lower/higher for high/low SFR galaxies at the same stellar mass.

(viii) This reverse or bimodality is more evident in Z -SSFR. Although this relation presents a high scatter, we can see clearly two populations of galaxies, one formed by low-mass galaxies showing an anticorrelation between SSFR and Z , and another population formed by massive galaxies showing a correlation between SSFR and Z .

(ix) It is clear from all the dependences that there is a different behaviour between low- and high-mass galaxies. To explain this, we generated a model based on the Z -SSFR relation. We propose that a combination of downsizing and different amount of neutral gas, can explain all our relationships and reverse observed. According to this model, for a given stellar mass, and due to different amounts of neutral gas, galaxies exhibit a wide range of SSFRs. The SSFR for the high-mass galaxies correlates with metallicity (the SSFR increases when Z increases). On the other hand, the SSFR of low-mass galaxies anticorrelates with Z (when the SSFR increases, the Z decreases). This opposite behaviour at the low- and high-mass ends explains the reverse found in the M_* - Z , M_* -SFR and M_* -SSFR relationships.

(x) We analysed the above dependences using different combinations of SFR and metallicities, such as Hopkins et al. (2003) and

Brinchmann et al. (2004) for the SFR, and Pettini & Pagel (2004), Tremonti et al. (2004) and Kewley & Dopita (2002) for the metallicity. In all the combinations, we found a strong dependence on the SFR for the M_* - Z relation, implying that this is independent of the method used.

ACKNOWLEDGEMENTS

GAMA is a joint European-Australasian project based around a spectroscopic campaign using the Anglo-Australian Telescope. The GAMA input catalogue is based on data taken from the Sloan Digital Sky Survey and the UKIRT Infrared Deep Sky Survey. Complementary imaging of the GAMA regions is being obtained by a number of independent survey programmes including *GALEX* MIS, VST KIDS, VISTA VIKING, *WISE*, *Herschel*-ATLAS, GMRT and ASKAP providing UV to radio coverage. GAMA is funded by the STFC (UK), the ARC (Australia), the AAO and the Participating Institutions. The GAMA website is <http://www.gama-survey.org/>. The work uses Sloan Digital Sky Survey (SDSS) data. Funding for the SDSS and SDSS-II was provided by the Alfred P. Sloan Foundation, the Participating Institutions, the National Science Foundation, the US Department of Energy, the National Aeronautics and Space Administration, the Japanese Monbukagakusho, the Max Planck Society and the Higher Education Funding Council for England. The SDSS was managed by the Astrophysical Research Consortium for the Participating Institutions. MAL thanks the ARC for a super science fellowship, and to the ‘Summer School in Statistics for Astronomers’, Center for Astrostatistics, PennState, for invaluable tutorials on ‘R’ and PCA.

REFERENCES

- Abazajian K. N. et al., 2009, *ApJS*, 182, 543
 Adelman-McCarthy J. K. et al., 2007, *ApJs*, 172, 634
 Asari N. V., Cid Fernandes R., Stasińska G., Torres-Papaqui J. P., Mateus A., Sodré L., Schoenell W., Gomes J. M., 2007, *MNRAS*, 381, 263
 Baldwin J., Phillips M., Terlevich R., 1981, *PASP*, 93, 5 (BPT)
 Bauer A. E., Drory N., Hill G. J., Feulner G., 2005, *ApJ*, 621, L89
 Bauer A. E. et al., 2013, preprint (arXiv:1306.2424)
 Bell E. F. et al., 2005, *ApJ*, 625, 23
 Brinchmann J., Ellis R. S., 2000, *ApJ*, 536, L77
 Brinchmann J., Charlot S., White S. D. M., Tremonti C., Kauffmann G., Heckman T., Brinkmann J., 2004, *MNRAS*, 351, 1151
 Brinchmann J., Pettini M., Charlot S., 2008, *MNRAS*, 385, 769
 Brooks A. M., Governato F., Booth C. M., Willman B., Gardner J. P., Wadsley J., Stinson G., Quinn T., 2007, *ApJ*, 655, L17
 Brough S. et al., 2011, *MNRAS*, 413, 1236
 Buat V. et al., 2008, *A&A*, 483, 107
 Calura F., Pipino A., Chiappini C., Matteucci F., Maiolino R., 2009, *A&A*, 504, 373
 Caputi K. I. et al., 2006, *ApJ*, 637, 727
 Cardelli J. A., Clayton G. C., Mathis J. S., 1989, *ApJ*, 345, 245
 Chabrier G., 2003, *PASP*, 115, 763
 Charlot S., Longhetti M., 2001, *MNRAS*, 323, 887
 Charlot S., Kauffmann G., Longhetti M., Tresse L., White S. D. M., Maddox S. J., Fall S. M., 2002, *MNRAS*, 330, 876
 Cid Fernandes R., Mateus A., Sodré L., Stasińska G., Gomes J. M., 2005, *MNRAS*, 358, 363
 Cid Fernandes R., Asari N. V., Sodré L., Stasińska G., Mateus A., Torres-Papaqui J. P., Schoenell W., 2007, *MNRAS*, 375, L16
 Cowie L. L., Songaila A., Hu E. M., Cohen J. G., 1996, *AJ*, 112, 839
 Davé R., Finlator K., Oppenheimer B. D., 2012, *MNRAS*, 421, 98
 De Lucia G., Kauffmann G., White S. D. M., 2004, *MNRAS*, 349, 1101
 Dekel A., Silk J., 1986, *ApJ*, 303, 39

- Dopita M. A., Periera L., Kewley L. J., Capacciolo M., 2002, *ApJS*, 143, 47
- Driver S. P. et al., 2011, *MNRAS*, 413, 971
- Efstathiou G., 2000, *MNRAS*, 317, 697
- Ellison S. L., Patton D. R., Simard L., McConnachie A. W., 2008, *ApJ*, 672, L107
- Erb D. K., Shapley A. E., Pettini M., Steidel C. C., Reddy N. A., Adelberger K. L., 2006, *ApJ*, 644, 813
- Feulner G., Gabasch A., Salvato M., Drory N., Hopp U., Bender R., 2005, *ApJ*, 633, L9
- Finlator K., Davé R., 2008, *MNRAS*, 385, 2181
- Foster C. et al., 2012, *A&A*, 547, A79
- Gavazzi G., Scodreggio M., 1996, *A&A*, 312, L29
- Gunawardhana M. L. P. et al., 2011, *MNRAS*, 415, 1647
- Gunn J. E. et al., 2006, *AJ*, 131, 2332
- Guzmán R., Gallego J., Koo D. C., Phillips A. C., Lowenthal J. D., Faber S. M., Illingworth G. D., Vogt N. P., 1997, *ApJ*, 489, 559
- Haas M. R., 2010, PhD thesis, University of Leiden
- Hammer F., Flores H., Elbaz D., Zheng X. Z., Liang Y. C., Cesarsky C., 2005, *A&A*, 430, 115
- Hopkins A. M. et al., 2003, *ApJ*, 599, 971
- Hopkins A. M. et al., 2013, *MNRAS*, 430, 2047
- Juneau S. et al., 2005, *ApJ*, 619, L135
- Kauffmann G. et al., 2003a, *MNRAS*, 346, 1055
- Kauffmann G. et al., 2003b, *MNRAS*, 341, 33
- Kelvin L. S. et al., 2011, *MNRAS*, 421, 1007
- Kelvin L. S. et al., 2012, *MNRAS*, 421, 1007
- Kewley L. J., Dopita M. A., 2002, *ApJS*, 142, 35
- Kewley L. J., Ellison S. L., 2008, *ApJ*, 681, 1183
- Kewley L. J., Dopita M. A., Sutherland R. S., Heisler C. A., Trevena J., 2001, *ApJ*, 556, 121
- Kewley L. J., Jansen R. A., Geller M. J., 2005, *PASP*, 117, 227
- Kobayashi C., Springel V., White S. D. M., 2007, *MNRAS*, 376, 1465
- Kroupa P., 2001, *MNRAS*, 322, 231
- Lara-López M. A. et al., 2009a, *A&A*, 493, L5
- Lara-López M. A., Cepa J., Bongiovanni A., Pérez, García A. M., Castañeda H., Fernández L. M., Pović M., Sánchez-Portal M., 2009b, *A&A*, 505, 529
- Lara-López M. A., Bongiovanni A., Cepa J., Pérez García A. M., Sánchez-Portal M., Castañeda H. O., Fernández Lorenzo M., Pović M., 2010a, *A&A*, 519, A31
- Lara-López M. A. et al., 2010b, *A&A*, 521, L53
- Lara-López M. A. et al., 2013a, preprint (arXiv:1304.3889)
- Lara-López M. A., López-Sánchez Á. R., Hopkins A. M., 2013b, *ApJ*, 764, 178
- Larson R. B., 1974, *MNRAS*, 169, 229
- Lequeux J., Peimbert M., Rayo J. F., Serrano A., Torres-Peimbert S., 1979, *A&A*, 80, 155
- Liang Y. C., Yin S. Y., Hammer F., Deng L. C., Flores H., Zhang B., 2006, *ApJ*, 652, 257
- López-Sánchez Á. R., 2010, *A&A*, 521, A63
- López-Sánchez Á. R., Esteban C., 2010, *A&A*, 517, 85
- López-Sánchez Á. R., Dopita M. A., Kewley L. J., Zahid H. J., Nicholls D. C., Scharwächter J., 2012, *MNRAS*, 426, 2630
- Mac Low M.-M., Ferrara A., 1999, *ApJ*, 513, 142
- Magrini L. et al., 2012, *MNRAS*, 427, 1075
- Maier C., Meisenheimer K., Hippelein H., 2004, *A&A*, 418, 475
- Maier C., Lilly S., Carollo C. M., Stockton A., Brodwin M., 2005, *ApJ*, 634, 849
- Maiolino R. et al., 2008, *A&A*, 488, 463
- Mannucci F., Cresci G., Maiolino R., Marconi A., Gnerucci A., 2010, *MNRAS*, 408, 2115
- Mateus A., Sodr e L., Cid Fernandes R., Stasińska G., Schoenell W., Gomes J. M., 2006, *MNRAS*, 370, 721
- Mouhcine M., Gibson B. K., Renda A., Kawata D., 2008, *A&A*, 486, 711
- Moustakas J., Kennicutt R. C., Jr, Tremonti C. A., 2006, *ApJ*, 642, 775
- Moustakas J., Kennicutt R. C., Jr, Tremonti C. A., Dale D. A., Smith J.-D. T., Calzetti D., 2010, *ApJS*, 190, 233
- Noeske K. G. et al., 2007, *ApJ*, 660, L43
- Papovich C. et al., 2006, *ApJ*, 640, 92
- Peebles M. S., Somerville R. S., 2013, *MNRAS*, 428, 1766
- Pérez-González P. G. et al., 2005, *ApJ*, 630, 82
- Pettini M., Pagel B. E. J., 2004, *MNRAS*, 348, L59
- Pilyugin L. S., Thuan T. X., 2011, *ApJ*, 726, L23
- Pilyugin L. S., Lara-Lopez M. A., Grebel E. K., Kehrig C., Zinchenko I. A., López-Sánchez Á. R., Vílchez J. M., Mattsson L., 2013, *MNRAS*, 432, 1217
- Reddy N. A., Steidel C. C., Fadda D., Yan L., Pettini M., Shapley A. E., Erb D. K., Adelberger K. L., 2006, *ApJ*, 644, 792
- Rodrigues M. et al., 2008, *A&A*, 492, 371
- Rosa-González D., Terlevich E., Terlevich R., 2002, *MNRAS*, 332, 283
- Rosales-Ortega F. F., Sánchez S. F., Iglesias-Páramo J., Díaz A. I., Vílchez J. M., Bland-Hawthorn J., Husemann B., Mast D., 2012, *ApJ*, 756, L31
- Salim S. et al., 2005, *ApJ*, 619, L39
- Sánchez S. F. et al., 2013, *A&A*, 554, A58
- Sarzi M. et al., 2006, *MNRAS*, 366, 1151
- Savaglio S. et al., 2005, *ApJ*, 635, 260
- Scannapieco C., Tissera P. B., White S. D. M., Springel V., 2008, *MNRAS*, 389, 1137
- Sharp R. et al., 2006, *Proc. SPIE Conf. Ser. Vol. 6269, Ground-based and Airborne Instrumentation for Astronomy*, SPIE, Bellingham, p. 62690G
- Simard L., Mendel J. T., Patton D. R., Ellison S. L., McConnachie A. W., 2011, *ApJS*, 196, 11
- Stoughton C. et al., 2002, *AJ*, 123, 485
- Strauss M. A. et al., 2002, *AJ*, 124, 1810
- Tassis K., Kravtsov A. V., Gnedin N. Y., 2008, *ApJ*, 672, 888
- Taylor E. N. et al., 2011, *MNRAS*, 418, 1587
- Tremonti C. A. et al., 2004, *ApJ*, 613, 898
- Vale Asari N., Stasińska G., Cid Fernandes R., Gomes J. M., Schlickmann M., Mateus A., Schoenell W., 2009, *MNRAS*, 396, L71
- Yates R. M., Kauffmann G., Guo Q., 2012, *MNRAS*, 422, 215
- Yin S. Y., Liang Y. C., Hammer F., Brinchmann J., Zhang B., Deng L. C., Flores H., 2007, *A&A*, 462, 535
- Zahid H. J., Yates R. M., Kewley L. J., Kudritzki R. P., 2013, *ApJ*, 763, 92

APPENDIX A: METALLICITY AND SFR CALIBRATIONS

We have calibrated the MPA–JHU metallicity and SFR with other methods using data from the SDSS. We have computed the PP04 metallicities for SDSS galaxies, and have calibrated them versus

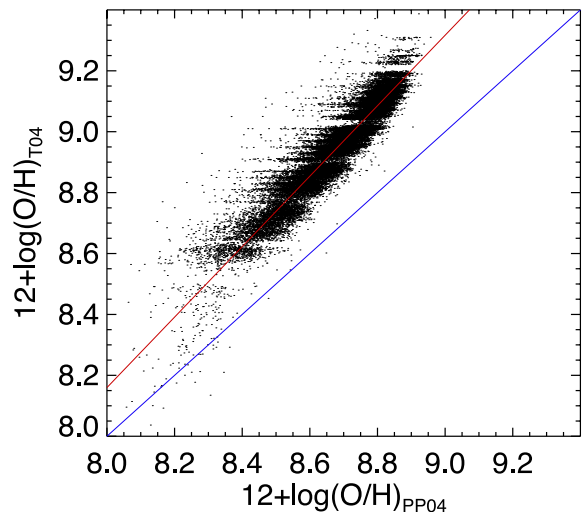


Figure A1. Metallicity calibration from the Pettini & Pagel (2004) method compared to the Tremonti et al. (2004) metallicities. The blue line shows the one to one relation, while the red line shows our calibration.

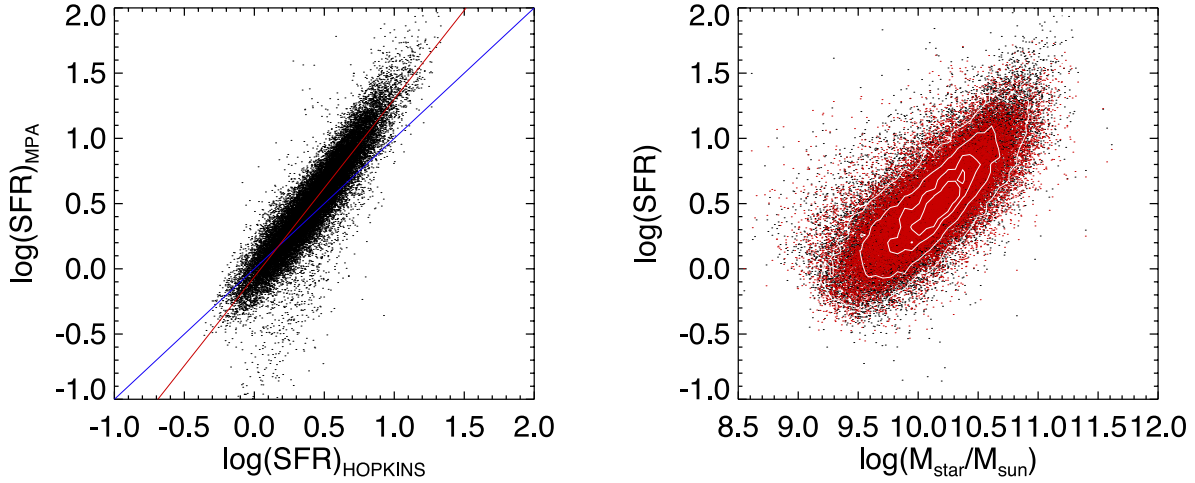


Figure A2. Left: SFR calibration from the Hopkins et al. (2003) to the Brinchmann et al. (2004) SFRs. Blue line shows the one to one relation, while red line shows our calibration. Right: M_{star} SFR relation using the Brinchmann et al. (2004) SFRs (black), and the recalibrated SFRs (red).

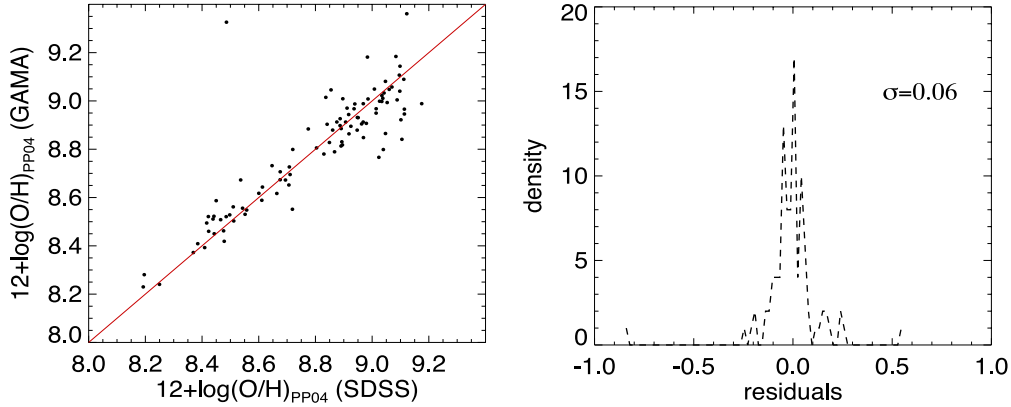


Figure B1. Left: comparison between GAMA and SDSS counterparts using the PP04 method, the red line corresponds to the one to one relation. Right: histogram of the residuals.

the T04 metallicities using a linear fit, as shown in Fig. A1. As a result, we obtained this calibration:

$$[12 + \log(\text{O}/\text{H})]_{\text{T04}} = -1.0962 + 1.1570 \times [12 + \log(\text{O}/\text{H})]_{\text{PP04}}. \quad (\text{A1})$$

We have also computed the Hopkins et al. (2003) SFRs for SDSS galaxies, and have calibrated them versus the Brinchmann et al. (2004) metallicities using a linear fit, as shown in Fig. A2. As a result, we obtained this calibration:

$$\log(\text{SFR})_{\text{B04}} = -0.064889 + 1.37597 \times \log(\text{SFR})_{\text{Hop}}. \quad (\text{A2})$$

APPENDIX B: GAMA AND SDSS COUNTERPARTS, A METALLICITY COMPARISON

A metallicity comparison has been done matching the GAMA phase-I with the SDSS-DR7 catalogues. From both surveys, metallicities have been estimated for the counterparts exactly in the same way using the PP04. The result is plotted in Fig. B1. There is good agreement between GAMA and SDSS with a sigma of the residuals of $\sigma = 0.06$.

This paper has been typeset from a $\text{\TeX}/\text{\LaTeX}$ file prepared by the author.